

EC PROJECT  
EVG1-CT-2002-00069



REL. I. E. F.



*RELIable Information on Earthquake Faulting*

Large Earthquake Faulting and Implications for the Seismic  
Hazard Assessment in Europe:  
*The Izmit-Duzce earthquake sequence of August-November 1999*  
*(Turkey, Mw 7.4, 7.1)*

# Hazard analysis and uncertainties of data

*Deliverable no. 26*  
*January 2006*

WP 6: Integration of multidisciplinary data for seismic hazard assessment  
WP 9: Multidisciplinary seismic hazard assessment

Prepared by M. B. Sørensen and K. Atakan

*PARTNER 6: Institutt for Geovitenskap, Universitetet i Bergen*



## **List of Contents**

Summary

1. Introduction

2. Seismic hazard analysis methods

    2.1. Probabilistic seismic hazard methods

    2.2. Ground motion simulation methodology

3. Uncertainties in seismic hazard analysis

    3.1. Uncertainties associated with the PSHA

    3.2. Sensitivity study on the ground motion simulations

4. Concluding remarks

Acknowledgements

References

## Summary

Within the framework of workpackage 6 (WP06) of the RELIEF project, multidisciplinary datasets are integrated for seismic hazard assessment. As a part of workpackage 9 (WP09), seismic hazard assessment is performed using two separate seismic hazard methodologies. The first one is conducted using probabilistic methods with poissonian and renewal models, and the other using a deterministic method with hybrid ground motion simulations based on scenario earthquakes. The uncertainties in the two different approaches are treated differently.

In order to quantify the uncertainties associated with the probabilistic methods, two separate studies are conducted for the Marmara region. One focuses on the effects of differences in source and the other on the attenuation models. An additional PSHA is conducted using a poissonian recurrence model. Results from these studies show significant differences in the absolute ground motion values, however the distribution is relatively similar for the case of the poissonian models. Significant differences also exist in the distribution of ground motion values when the poissonian PSHA results are compared with the time dependent models.

The uncertainties associated with the ground motion simulations are quantified by comparing various input scenarios with respect to a “standard scenario” as described in RELIEF Deliverable # 25. Comparisons indicate clearly that critical parameters such as the rupture initiation point, rupture velocity, rise time and the stress drop have significant effect on the resulting ground motions.

## 1. Introduction

The city of Istanbul is subject to a significant seismic hazard due to its close proximity to the Marmara Sea segment of the North Anatolian Fault (NAF) (Figure 1.1). During the last century there has been a westward migration of large, destructive earthquakes along the NAF with the latest events occurring in Izmit and Duzce in 1999 (e.g. Barka et al., 1999). Following these large earthquakes, there has been an increase in the coulomb stress along the Marmara Sea segment (Hubert-Ferrari et al., 2000) which, together with the fact that no large earthquakes have occurred at least since 1766 (Barka et al., 2002), indicates that a large earthquake is likely to break this part of the NAF within the life time of the present city environment (Parsons et al., 2000; Parsons, 2004).

For future risk mitigation and city planning, a reliable estimate of the seismic hazard in Istanbul is needed. Seismic hazard in Istanbul has previously been estimated using probabilistic methods (Atakan et al., 2002; Erdik et al., 2004). Recently however, increased knowledge on the NAF within the Marmara Sea allowed other methods to be applied. Pulido et al. (2004) modeled the bedrock ground motions due to a finite extent scenario earthquake source ( $M=7.5$ ) in the Marmara Sea using a hybrid broadband simulation technique, and thereby gave a first insight to the complexity of ground shaking to be expected in a future earthquake. Such results are important due to their direct engineering implications. However, the uncertainties related to defining the source parameters of a scenario earthquake influence the scenario result in a way which is until now not well resolved. Our main objective in this report is therefore to study and quantify the effect of these uncertainties.

The uncertainties associated with the probabilistic methods were presented in earlier deliverables (RELIEF - UiB Deliverable 18) and therefore will only be briefly mentioned here. In the present study we focus on the hybrid ground motion simulations due to a number of earthquake scenarios in the Marmara Sea and compare to a ‘standard’ scenario. The various scenarios (16 in total) are defined by changing the critical source parameters one at a time to see their influence on the simulated ground motions. This provides important information about the sensitivity of the ground motions to the different source parameters and reveals the most critical ones.

## **2. Seismic hazard analysis methods**

Seismic hazard analyses for the Marmara region are conducted using two separate approaches. First the seismic hazard is estimated using the standard probabilistic methods including poissonian and renewal models. Secondly, ground motions are simulated based on various scenario earthquakes using complex physical source models. In the following these methods are described in more detail.

### **2.1. Probabilistic seismic hazard methods**

The first study follows the methodology used by Atakan et al. (2002). The probabilistic seismic hazard analysis was performed using 12 different input models, based on a combination of three earthquake source models and four attenuation relations. The three earthquake source models were one based on a standard poissonian assumption (Cornell, 1968) and two based on a renewal model (McGuire, 1993) assuming a ‘characteristic earthquake’ (Schwartz and Coppersmith, 1984; Youngs

and Coppersmith, 1985). In the renewal models the time elapsed since the last event is incorporated, recognizing that the stress accumulation and release process on faults is cyclical (McGuire, 1993). In each of these models, four different attenuation relations were applied. These are from Ambraseys et al. (1996), Boore et al. (1997), Campbell (1997) and Sadigh et al. (1997). Results are presented in 12 different maps showing PGA with a 10% probability of exceedance in 50 years for bedrock conditions. The earthquake source area as well as the area used for the computations are shown in Figure 2.1.1. The computations were performed using the CRISIS99 software (Ordaz, 1999), and the results are contoured and presented without any additional smoothing, except the extrapolations done during the computational procedures. CRISIS99 has the same basic capabilities as the older, more widely used programs, such as the EQRISK (McGuire, 1976) and SEISRISK III (Bender and Perkins, 1987). In addition it is possible to compute the conditional probability of occurrence for a renewal model using the time elapsed since the last occurrence of a ‘characteristic earthquake’. Source geometry can be modeled either as a Poisson or a ‘characteristic earthquake’ process. For the Poissonian assumption, magnitude-frequency relations are smoothly truncated Gutenberg-Richter curves, whereas for the characteristic earthquake assumption, the program assumes a Gaussian distribution of magnitudes. Hazard computations are performed simultaneously for several ground motion measures (for instance, maximum acceleration, velocity and several spectral ordinates). Required attenuation laws are given in the form of tables containing the median values of the ground motion measures as a function of magnitude and focal distance. Spatial integrations are performed using a recursive triangularization algorithm, optimizing the number of calculations (i.e. it integrates with more points for the nearest sources and less points for distant sources).

The earthquake catalogue used is from the International Seismological Centre (ISC) for the modern instrumental part (1964-present) (Figure 2.1.1a). The historical earthquake catalogue used relies basically on the work of Ambraseys and Finkel (1995) for the period 1500 until 1800. The catalogue compiled by Eyidogan et al. (1991) is used for the 19<sup>th</sup> century.

Three assumed earthquake source models are shown in Figure 2.1.1. In Model 1, we assumed a poissonian earthquake occurrence and used area sources similar to those previously applied by Erdik et al. (1999) (Figure 2.1.1b). This is chosen in order to calibrate our results with the previous ones. In Models 2 and 3, we assumed renewal earthquake occurrence and delineated two alternative source zonations, as shown in Figures 2.1.1c and 2.1.1d. Model 2 assumes broader source zones in the Marmara Sea, as opposed to the Model 3 where the sources are defined based on the assumption

that a narrow fault zone cuts across the three basins in the Marmara Sea (Kuscu et al., 2000). The source zones as well as the earthquake input parameters are similar to those defined in Atakan et al. (2002). A comparison between the four attenuation relations is shown in Figure 2.1.2. Here it is seen that the Ambraseys et al. (1996) and Sadigh et al. (1997) relations represent high ground motion levels at distances less than 50 km (for more details, see Atakan et al. (2002)).

## **2.2. Ground motion simulation methodology**

We follow the approach of Pulido and Kubo (2004) and Pulido et al. (2004), using a hybrid method for modeling the ground motion. This procedure combines a deterministic simulation at low frequencies (0.1-1 Hz) with a semi-stochastic simulation at high frequencies (1-10 Hz). A finite-extent scenario earthquake source embedded in a flat-layered 1D velocity structure is assumed. The source consists of a number of asperities, which are divided into subfaults assumed to be point sources. The total ground motion at a given site is obtained by summing the contributions from the different subfaults. For the low frequencies, subfault contributions are calculated using discrete wave number theory (Bouchon, 1981) and summed assuming a given rupture velocity. At high frequencies, the subfault contributions are calculated using the stochastic method of Boore (1983) and summed using the empirical Greens function method of Irikura (1986). The radiation pattern is changed from a theoretical double-couple radiation pattern at low frequencies to a uniform radiation pattern at high frequencies following Pulido and Kubo (2004).

The ground motion simulations are performed at bedrock level and therefore do not take local site effects into account. This is important to keep in mind when interpreting the simulation results since local site effects are indeed present and important, especially in the southwestern part of the city (e.g. Birgören et al., 2004; Sørensen et al., in review). This issue is being addressed by Sørensen et al. (in review), aiming to combine ground motion simulation results with information about local site effects.

As input for the modelling, the source needs to be defined in terms of the location of the rupturing fault and its asperities together with asperity parameters such as rise time, rupture velocity, stress drop and seismic moment. Also the properties of the surrounding crust need to be defined giving velocity structure and attenuation characteristics.

### **3. Uncertainties in seismic hazard analysis**

In general, uncertainties in probabilistic seismic hazard assessment are divided into two groups; epistemic and aleatory. The epistemic uncertainties are usually introduced due to the variations in the input parameters. These can be improved by additional data and can be quantified in terms of standard deviations. However, the aleatory uncertainties are related to the understanding of the phenomenon and if the applied concept is wrong, additional data do not necessarily improve the reliability. It is therefore more difficult to quantify these aleatory uncertainties.

In the following two sections, the uncertainties associated with the probabilistic and deterministic (ground motion simulations) seismic hazard assessments are given separately. Since most of the discussion on the uncertainties regarding the PSHA were already given in previous deliverables (see RELIEF – UiB Deliverables 16 and 18), more emphasis is given to the sensitivity analysis performed on the ground motion simulations.

#### **3.1. Uncertainties associated with the probabilistic seismic hazard assessments**

Uncertainties associated with the probabilistic hazard analyses conducted during the RELIEF project are treated in four categories. These are the uncertainties associated with; (i) earthquake catalogues, (ii) earthquake recurrence models, (iii) earthquake source zonation, and (iv) attenuation of ground motion. These uncertainties are investigated by applying different input sets and the resulting probabilistic hazard maps were already presented. The reader is referred to the RELIEF – UiB Deliverables 16 and 18, for details. Here, for comparison, we only present the probabilistic hazard maps with different attenuation relations (Figures 3.1.1 and 3.1.3).

Even though several attenuation relationships can be argued to be valid for the Marmara Sea region, these give different hazard levels when used as input in a probabilistic seismic hazard study. It is therefore necessary to establish a local relationship based on the available data. The available strong motion recordings from the region are limited and therefore regressions are performed on weak motion data. These results are presented in a separate paper by Akinci et al., (in press) (see Appendix II of the RELIEF-UiB Annual Report for 2005). The seismic hazard studies for the Marmara Sea region show that the city of Istanbul is under a significant hazard of strong ground

shaking. Ground motion maps for a 10 % probability of exceedence in 50 years show that ground motion levels as high as 0.4g are possible.

### **3.2. Sensitivity analysis on the ground motion simulations**

The first step in performing the ground motion simulations is to set up an earthquake scenario along the Marmara segment of North Anatolian Fault (NAF). The NAF is a ca 1200 km long fault structure extending through the northern part of Turkey from Erzincan in the East to the Aegean Sea in the West. The structure forms the boundary between the westward moving Anatolian Block with respect to the Eurasian plate, accommodating the relative motion through right-lateral strike-slip motion. In the westernmost part, around the Marmara Sea, the NAF splits into two main branches (Figure 1.1). Studying GPS displacement vectors, Okay et al. (2000) showed that the main strain accumulation takes place along the northernmost fault branch, which is therefore the target of our ground motion modeling. This northernmost fault branch consists of two main segments, namely the Central Marmara Fault (CMF) and the North Boundary Fault (NBF). The CMF has a strike almost parallel to the general stress orientation in the region and is therefore expected to break in a pure strike-slip earthquake. The NBF, on the other hand, is oblique to the stress orientation and constitutes a releasing bend on the NAF. We therefore expect an oblique normal mechanism along this segment. The velocity of the regional plate motion is approximately 2 cm/yr (Straub et al., 1997). Major historic earthquakes along these segments of the NAF include the 1509 earthquake (M=7.2) and the 1766 earthquake sequence (M=7.1 and M=7.4). In addition, a M=6.4 earthquake has ruptured along the NBF in 1963 (Ambraseys and Jackson, 2000).

#### ***Input scenarios***

In order to provide a comparison between the different scenario results we have defined a ‘standard scenario’. The details of this scenario are explained below. The location and dimensions of the rupturing fault are defined by considering the local tectonics and seismicity. We assume a combined rupture of the CMF and NBF segments of the NAF. A total fault length of 130 km is used, which is confined to the area between the 1999 Izmit rupture to the east and the 1912 Ganos rupture to the west (Figure 1.1). We assume a fault width of 20 km in agreement with the depth of the seismogenic zone as indicated by the depth distribution of seismicity (Gurbuz et al., 2000). The fault plane solution used is the one of Pulido et al. (2004) with pure right-lateral strike-slip faulting along the CMF and an oblique-normal mechanism along the NBF. Two asperities are defined

covering 22% of the fault plane following the empirical results of Somerville et al. (1999). These are located near the intersection of the CMF and NBF segments (Figure 1.1). This area has previously been suggested to be a seismic gap (Gurbuz et al., 2000), characterized by its low seismicity. The seismic moment released by the scenario earthquake is  $2.0 \times 10^{20}$  Nm, which is an average value of the seismic moments estimated by different authors for the 1999 Izmit earthquake (Pulido et al., 2004). The velocity model used in the modelling is the one used for routine location of earthquakes in the region (Figure 3.2.1). For the cut-off frequency  $f_{\max}$  we use a value of 10 Hz, which is also the upper frequency limit of the calculations. In practice this implies that the high-frequency decay of the ground motion is mainly controlled by attenuation.

For the standard scenario, the rupture initiation point is located in the westernmost edge of asperity 1 (Figure 1.1). This is believed to be a likely location since the boarder regions of asperities represent significant changes in physical properties of the fault and thereby zones of weakness. Based on seismic moment, fault area and asperity area, the stress drop is calculated based on the relations of Das and Kostrov (1986) and Brune (1970) following Pulido et al. (2004). Rupture velocity and rise time are taken from Pulido et al. (2004) for the standard scenario. The regional attenuation is defined in terms of Q. For the standard scenario we have used the “Low Attenuation Model” of Pulido et al. (2004). The source parameters of the standard scenario are summarized in Table 1. It should be noted that the standard scenario is considered as a conservative approximation.

**Table 1:** Source parameters for the standard scenario.

Seismic moment	$M_0 = 2.0 \cdot 10^{20}$ Nm
Strike / Dip / Slip CMF segment	81.5 / 90 / 180
Strike / Dip / Slip NBF segment	110 / 90 / -135
Average stress drop	5.0 MPa
Asperity stress drop	10 MPa
Rise time	3.0 s
Rupture velocity	3.0 km/s
$f_{\max}$	10 Hz
Q	$100 \cdot f^{1.5}$

Based on the standard scenario, we have changed source parameters one by one in order to test the effect on the ground motions. The parameters, which have been tested, are: low-frequency attenuation ( $Q_p$  and  $Q_s$ ), high-frequency attenuation (Q), rise time, rupture velocity, rupture

initiation point and stress drop. In total, 16 “test scenarios” have been investigated, which are listed in Table 2.

**Table 2:** Scenarios which have been tested in this study.  
Only the parameter differing from the standard scenario is listed.

Scenario 1a	$Q_p$ and $Q_s$ reduced by 50%
Scenario 1b	$Q = 100 \cdot f^{0.5}$
Scenario 1c	$Q = 250 \cdot f^{1.5}$
Scenario 1d	$Q = 250 \cdot f^{0.5}$
Scenario 2a	Rise time 2.0 s
Scenario 2b	Rise time 4.0 s
Scenario 2c	Rise time random $3 \pm 1$ s
Scenario 3a	Rupture velocity 2.5 km/s
Scenario 3b	Rupture velocity 3.5 km/s
Scenario 3c	Rupture velocity random $3 \pm 0.5$ km/s
Scenario 4a	Rupture initiation at western edge of CMF
Scenario 4b	Rupture initiation at intersection of CMF and NBF
Scenario 4c	Rupture initiation at eastern edge of asperity 2
Scenario 4d	Rupture initiation at eastern edge of NBF
Scenario 5a	Stress drop asperity: 5 MPa, background: 2.5 MPa
Scenario 5b	Stress drop asperity: 15 MPa, background: 7.5 MPa

### *Simulation results*

The simulated PGA and PGV values for the standard scenario are shown in Figure 3.2.2. The largest accelerations are predicted in the southernmost part of the city, which is also located closest to the rupturing fault. Here we can expect bedrock accelerations of 0.5g or more in some places. There is a very strong forward directivity effect on the ground motions, which is especially evident in the PGV distribution. Largest velocities are expected in the southeastern part of the city, where we predict velocities up to 125 cm/s. Due to the forward directivity, the shaking is extended far towards East from the rupturing fault which may have important implications along the populated areas around the Izmit gulf.

For the 16 test scenarios, composite plots have been made to show the ground motion distributions as presented in Figures 3.2.3-3.2.18. In order to provide an easy comparison to the standard scenario, the absolute difference of peak ground motion between a given scenario and the standard

scenario are shown in separate plots. In total there are four plots in each figure corresponding to a scenario (i.e. absolute PGA and PGV and difference in PGA and PGV).

In scenario 1a, the low frequency attenuation factors ( $Q_p$  and  $Q_s$ ) have been reduced by 50 %. The exact values of  $Q_p$  and  $Q_s$  for the standard scenario and scenario 1a are given in Table 3. The effect seems to be very small for both the PGA and PGV values (Figure 3.2.3). The main difference is seen in the direction of forward directivity, where both PGA and PGV reduce slightly.

**Table 3:** Low frequency attenuation parameters used in standard scenario and scenario 1a.

Depth (top of layer)	Standard scenario		Scenario 1a	
	$Q_p$	$Q_s$	$Q_p$	$Q_s$
0 km	360	180	180	90
2 km	550	275	275	137.5
15 km	650	325	325	162.5
40 km	700	350	350	175

In scenarios 1b and 1c we have tested the effect of high frequency attenuation by varying  $Q$ . In the ground motion simulations we use a frequency dependent  $Q$  defined by a relationship of the form  $Q=Q_0 \cdot f^a$ . In scenario 1b (Figure 3.2.4) we change the frequency dependency of the attenuation,  $a$ , using a factor of 0.5 (1.5 for standard scenario). This implies lower values of  $Q$  for the higher frequencies, which implies higher attenuation of the seismic waves. On the other hand we will see an increase of  $Q$  for the low frequencies implying lower attenuation. In scenario 1c (Figure 3.2.5) we increase  $Q_0$  to a value of 250 (100 for standard scenario). This causes a general increase of  $Q$ , which implies reduced attenuation. The simulation results are in agreement with these considerations. For scenario 1b we see a reduction of PGA over a large area with a magnitude of up to 0.35g in comparison to the standard scenario. For the PGVs, the effect is smaller (maximum difference of 35 cm/s compared to standard scenario), but there is a tendency of increased PGVs in the forward directivity direction and decreased PGVs in the backward directivity direction. For scenario 1c there is a general increase in PGA over the study area with a magnitude of up to 1g. The effect on PGV is mainly in the distribution of the ground motions. At asperity 1 there is a strong increase in PGV whereas the PGV decreases further eastwards at asperity 2, maximum change is at the order of 100 cm/s. Little effect is seen away from the fault. For the sake of comparison we have run a third scenario (scenario 1d, Figure 3.2.6) using the attenuation relationship  $Q=250 \cdot f^{0.5}$ , which is a combination of scenarios 1b and 1c as is reflected in the results. The effect of using this attenuation relation is an increase in PGA (up to 0.15g) distributed over a large area around the

ruptured fault. The effect on the PGVs is similar to what is seen for scenario 1c, with decreased velocities in the forward directivity direction and increased velocities in the backward directivity direction, but the effect is spread over a larger area. This indicates that the frequency dependency (a) has the largest effect on the high-frequency ground motion (controlling acceleration) whereas  $Q_0$  has the main effect on the low-frequency ground motion (controlling velocity).

In scenarios 2a-c (Figures 3.2.7-3.2.9), the influence of the rise time on the ground motion was tested by simulating with rise times of 2 s (scenario 2a, Figure 3.2.7), 4 s (scenario 2b, Figure 3.2.8) and randomly varying between 2-4 s (scenario 2c, Figure 3.2.9) and comparing to the standard scenario with a rise time of 3s. The effect of the rise time on the PGVs is clear. Increasing the rise time decreases the PGV and vice versa. The effect is most dominating close to the asperities of the fault plane where we see a change of up to 170 cm/s relative to the standard scenario, but also spreads away from the fault, especially in the direction of forward directivity. The effect of using a randomly varying rise time is significantly smaller (change up to 10 cm/s) and more complex (Figure 3.2.9). The general trend is a reduction of PGV in the near field and an increase in the far field. The effect on the PGAs is more scattered and diffuse. The general trend is a scattered reduction in PGA for both reduced and increased rise time with the largest impact close to the asperities. However, the reduced rise time in scenario 2a causes significant increase of PGA at parts of the asperities. Letting the rise time vary randomly causes a reduction in PGA close to what is observed when increasing the rise time. In all cases, the maximum level of change is 0.5-0.6g.

In scenarios 3a-c, the effect of the rupture velocity has been tested. In scenario 3a (Figure 3.2.10), the rupture velocity was reduced to 2.5 km/s (3.0 km/s for standard scenario), in scenario 3b (Figure 3.2.11) it was increased to 3.5 km/s and in scenario 3c (Figure 3.2.12) we let the rupture velocity vary randomly between 2.5-3.5 km/s. The simulation results show that the rupture velocity has a strong effect on the PGVs, especially in the forward directivity direction. Increasing the rupture velocity also increases the PGV, whereas a reduction in rupture velocity causes reduced PGVs. Using the randomly varying rupture velocity causes a change in the PGV distribution with areas with increased PGV being the dominating feature. The level of change for the PGV is up to 150 cm/s. For the PGAs the effect of changing rupture velocity is more scattered and affects a larger area also away from the direction of forward directivity. Reduction of rupture velocity reduces the PGAs whereas the picture for increased rupture velocity is more complex with significant increases in PGA in many areas. However, dominating patches of reduced PGA also exist. Using a random rupture velocity causes a general reduction in PGA in patches scattered in a large area around the

rupturing fault. The level of maximum change for the PGAs is 0.6-0.7g or even higher in the region close to asperity 1 for scenario 3a.

The effect of changing the location of rupture initiation has been tested in scenarios 4a-d. In scenario 4a (Figure 3.2.13), the rupture initiation point (RIP) was moved westwards to the westernmost point of the CMF. In scenario 4b (Figure 3.2.14), the RIP was moved to the intersection of the CMF and NBF segments of the rupturing fault. In scenario 4c (Figure 3.2.15), the RIP was located at the easternmost point of asperity 2 and for scenario 4d (Figure 3.2.16) the RIP was located at the easternmost point of the NBF segment. For all these scenarios, the hypocentral depth was held constant at 15 km for easy comparison. The simulation results show a clear effect of the location of the RIP on the distribution of the ground motion. For the PGVs, the effect of directivity is very clear and significant. For scenario 4a, moving the RIP westwards increases the significance of the central part of the CMF whereas the westernmost part has reduced PGVs due to the directivity towards this region in the bilateral rupture of the standard scenario. PGV also decreases in the region around asperity 1 and in the forward directivity direction of the standard scenario. This is due to the longer distance to the RIP. For scenario 4b we again see a reduction of PGV in the forward directivity direction of the standard scenario, but in this case the reduction is due to the changed direction of the rupture along asperity 1. This also causes an increase in PGV towards the west. The same trend is seen more clearly for scenarios 4c and 4d where the RIP is moved successively longer eastward. This completely changes the directivity pattern causing reduced PGVs to the east and increased PGVs to the west. The magnitude of the change is up to 300 cm/s in all cases except scenario 4a where PGV changes on the order of 100 cm/s. For the PGA distribution, the same trend is present, but with more scatter due to the more unstable nature of accelerations. The largest changes are observed close to the RIP of the standard scenario. The maximum magnitude of the variation varies between 0.4-0.7g for the four scenarios.

The final test of this study was for the influence of stress drop on the ground motion distributions in scenarios 5a-b. In scenario 5a (Figure 3.2.17), the stress drop was reduced by 50% to 2.5 MPa for the background slip and 5 MPa for the asperities. In scenario 5b (Figure 3.2.18), the stress drop was increased by 50% to 7.5 MPa for the background slip and 15 MPa for the asperities. The effect is most significant on the PGA levels. Both PGV and PGA decrease when decreasing the stress drop and increase for an increased stress drop, affecting a large area around the rupturing fault. The magnitude of the change is 30-40 cm/s for PGV and up to 0.5g for PGA.

As shown above, several of the input parameters used in the ground motion simulations have a significant effect on the resulting ground motions, both in terms of distribution and absolute level of the ground motions. The location of the rupture initiation is critical due to the effects of directivity and, for the case of Istanbul, controls the distribution of very strong shaking in the densely populated areas of the city centre vs. offshore in the Marmara Sea.

The magnitudes of changes caused by varying the rise time and rupture velocity are on the same level. However, the nature of the changes are different in terms of the affected regions. The rise time mainly affects the asperities where most of the slip occurs, but the effect also tends to be distributed in the direction of rupture propagation. The rupture velocity, on the other hand, has an important effect along the whole rupture and the largest variations are seen along the forward directivity direction. In both cases the effect on PGA is scattered and in general distributed over larger regions than the PGVs.

### ***Frequency distribution of ground motion and implications for engineering***

When applying seismic hazard results to engineering problems, the frequency distribution of the ground motions becomes an important factor in addition to the ground motion levels. Therefore we have studied the frequency distribution of the ground motion simulation results at six sites in terms of spectral acceleration (SA), spectral velocity (SV) and response spectra. The locations of the sites (Figure 3.2.19) have been chosen to represent different parts of the city both in terms of land use, local geology and directivity of the simulated ground motions. Site 162 is located on the Asian side of the city in the forward directivity direction for the standard scenario. Site 244 is in the northernmost part of the city at the Black Sea coast and is included for investigating the effect of distance on the spectra. Sites 178 (Avcilar) and 179 (Ataköy) are located in areas known to be affected by local site effects (Tezcan et al., 2002, Sørensen et al., in review). The remaining two sites, 275 and 276, are located in the historical center (Sultanahmet) and the business center (Levent), respectively.

For each of the six sites, SA and SV have been averaged in four frequency bands, namely  $f < 1\text{Hz}$ ,  $1\text{Hz} < f < 3\text{Hz}$ ,  $3\text{Hz} < f < 5\text{Hz}$  and  $f > 5\text{Hz}$ . The limits of these frequency bands are chosen to coincide with the corner frequencies in the Turkish Design Code for various site classes (Aydinoglu, 1998). A large part of the building stock in Istanbul consists of 3-5 story buildings with resonance frequencies around 3-5 Hz. However, also a large number of high-rise buildings susceptible to

frequencies down to 1 Hz are present. Shaking at frequencies lower than 1 Hz affects mainly very high-rise or long-span structures and therefore has less engineering implications in most parts of the city. Figures 3.2.20-23 show the comparisons of spectral values for each of the six sites. For each site, average SAs and SVs are computed for the standard scenario and each of the 16 test scenarios, and the absolute values are compared in histogram plots. Results are very similar for SA and SV and therefore only results for SV are shown.

For the low frequencies, the most dominating parameters are rise time and rupture velocity (scenarios 2a-c and 3a-c). The influence of the rise time is significant at all the sites, whereas rupture velocity has little effect at the northernmost site (site 244), indicating that the effect of rupture velocity is only significant within a given critical distance. At higher frequencies, the variations in SA and SV for these scenarios are negligible, indicating that even though these parameters cause large variations in the ground motion levels, their effect for engineering issues is limited in most parts of the town.

In the 1-3Hz frequency band we see an effect of the rupture initiation point on the spectral values. This variation is smaller at the higher frequencies, and the RIP therefore mainly has an impact on the damage of large structures such as high-rise buildings. Another outstanding feature for this frequency band is the stress drop, which has a clear effect on the spectral values in all frequency bands above 1Hz. From this we can conclude that the stress drop is an important parameter with large impact on the level of damaging ground motion, which therefore should be given attention in future studies. In the highest frequency bands, the effect of a in the frequency dependent  $Q$  ( $Q=Q_0 \cdot f^a$ ), is obvious.

In Figures 3.2.20-23, the SA and SV values are plotted for the EW and the NS components separately. For the high frequencies, the amplitudes are almost identical for the two components, which is in agreement with the radiation pattern correction applied in the simulations (isotropic radiation pattern at high frequencies). However, at lower frequencies large differences are seen, especially in the forward directivity direction (site 162), which are probably a combined effect of the directivity and the double couple radiation of the low-frequency energy from the fault.

Figure 3.2.24 shows velocity response spectra for the standard scenario at the six sites of Figure 3.2.19. It is seen that both peak frequency and spectral level varies with azimuth and distance to the fault. At site 162 (Figure 3.2.24a) we see a very strong peak at long periods (low frequencies) in the

fault parallel direction. This is expected to be due to the forward directivity of the ground motion. In general, at this site, we see maximum response spectra values at 0.2-0.3 Hz frequencies, which will have an effect on high-rise buildings in this area. Secondary peaks are seen around 2 Hz and 5 Hz, which will have a smaller absolute effect, but will affect lower rise buildings which are more common.

The response spectra for sites 178 and 179 (Figure 3.2.24b and 24c) are very similar, and differ significantly from the spectra at site 162. For these spectra we see a strong peak around 2 Hz which will be very critical for building damage in these densely populated areas largely occupied by ~5 story buildings, which have resonance frequencies around this value (Aydinoglu, 1998). Since we expect significant site effects in this area with amplification also around this frequency (Sørensen et al., in review), the actual response can be even higher than predicted in this study. Again we also see peaks around 0.2 and 0.5 Hz which can affect high-rise buildings.

Site 244 (Figure 3.2.24d) is located far from the rupturing fault, which is also reflected in the response spectra having significantly lower values. The dominating peak is at low frequencies, 0.2-0.3 Hz, but also here amplitudes are low and little effect is predicted.

At site 275 (Figure 3.2.24e), the Sultanahmet site, we also see a main peak at 0.2 Hz and a strong secondary peak at ca 2 Hz. This secondary peak will be critical for the building stock mainly consisting of old residential blocks of around 5 stories. The large number of historical monuments have much more complex response than simple quadratic modern residential buildings and may be vulnerable to a variety of frequency bands.

Finally, for the site 276 (Figure 3.2.24f) located in the business district of Istanbul, the strongest velocity response is seen at low frequencies (0.2-0.3 Hz) which is critical for the many high-rise buildings (40 stories and more) present in this area.

From an engineering perspective, an important result of the sensitivity analysis of this study is the effect of changing the scenario input parameters on the resulting response spectra. In order to explore this in detail, response spectra from all 17 scenarios at the six sites have been plotted together in Figure 3.2.25. In this figure we see that despite the large variations between the various scenarios in terms of ground motion levels and distributions, the response spectra are relatively similar for most scenarios. The general trend is that the variation increases for the low frequencies.

For the peak frequencies we see a significant variation up to  $\pm 50\%$ , but this is only seen for a few scenarios. Generally, the variation between the response spectra is larger for sites close to the fault (Sites 178 and 179 in Figures 3.2.25b and 25c), whereas much smaller variations are seen at larger distances (sites 244 and 276 in Figures 3.2.25d and 25f). The similarity between the response spectra implies that even if we are uncertain of the exact values of the input parameters for ground motion modeling, we still do a reasonably good job in predicting consistent response spectra which are, at the end, maybe the most useful result of these models in terms of earthquake risk mitigation.

The standard deviation of PGA and PGV have been computed for all simulation points based on the 16 scenarios and their spatial distribution is shown in two maps (Figures 3.2.26 and 27, for PGA and PGV respectively). In general these two maps indicate that the largest variation in the standard deviation occurs close to the asperities. This is as expected since much of the variation in the ground motion is associated to the location of asperities and their input parameters. Their variation naturally affects the surrounding regions. The level of standard deviation decreases gradually by increasing distance from the fault asperities.

### ***Discussion***

The results of this study reveal that even if we have reliable ground motion estimation methodologies we are still limited in the prediction of ground motions from future earthquakes by our limited knowledge of the source parameters. This uncertainty is important and should always be kept in mind when interpreting ground motion simulation results. However, being aware of the uncertainties, ground motion simulations still provide a strong tool in determining seismic hazard levels in places where there is no doubt that a large earthquake will strike and the gain from probabilistic seismic hazard analyses therefore is limited.

When modeling ground motions from future earthquakes, a useful approach is to define a number of scenarios with different values of the uncertain source parameters. For example, a “worst-case scenario” and a “best-case scenario” can be defined. In this way, upper and lower limits of the expected ground motions can be defined and the user can choose the appropriate level of conservatism depending of the use of the results.

The most important parameters for the ground motion modeling, in terms of ground shaking levels, are location of the rupture initiation, stress drop, rise time, rupture velocity and the high-frequency

attenuation relation used for the studied region. However, the impact of these parameters in frequency bands of engineering interest varies. From an engineering perspective, the most important parameters are the stress drop and the location of rupture initiation. Unfortunately, these parameters are difficult to predict for future earthquakes, but detailed studies should be made ahead of ground motion modeling, and in case of large uncertainties, extreme values should be input to the models to set bounds on the predicted ground motions.

In the present study we have used one of many methodologies for estimating ground motions due to a future large earthquake. We have tested the effect of changing the various input parameters but have not discussed the issue of variation among different ground motion modeling methodologies. We feel that this discussion is out of the scope of this paper where our aim is to get closer to a realistic scenario ground motion for Istanbul and therefore we focus only on the application of one method.

#### **4. Concluding remarks**

Based on our analyses of the uncertainties in the PSHA and the effect of input parameters on ground motion simulation results we can draw the following conclusions:

- Seismic hazard assessment based on ground motion simulations are more appropriate when compared to the probabilistic seismic hazard assessments, since the expected hazard for the city of Istanbul is controlled by the NAF in the Marmara Sea where the next large earthquake is expected to occur.
- Ground motion simulations using physically based complex earthquake source models provide a more detailed picture of the ground motion distribution in the area when compared to the PSHA.
- The largest uncertainty associated with the PSHA is due to the choice of the attenuation relationship for the Marmara Sea region. The resulting hazard levels vary depending upon the chosen relationship. Other sources of uncertainties are those associated with the seismic source zonation as well as the choice of the earthquake recurrence models.
- Based on our analysis of the effect of input parameters on ground motion simulation results the effect of a M=7.5 earthquake in the Marmara Sea on the city of Istanbul will be significant with the largest ground motions occurring in the southern and southeastern parts of the city. Here, ground accelerations at the level of 0.5g can be expected at bedrock level.

These acceleration levels in general slightly larger than those expected based on the PSHA results.

- The level and distribution of modeled ground motions are highly dependent on the input source parameters and these uncertainties should be taken into account when applying modeling results. In this respect modeling for both ‘worst-case’ and ‘best-case’ scenarios provide the upper and lower bounds on the expected ground motions.
- Stress drop, rise time, rupture velocity, and rupture initiation point are the most significant parameters in terms of variations in ground shaking levels (Figures 4.1 – 4.5). However these parameters have their effect in different frequency bands and the engineering significance therefore varies.
- From an engineering point of view, stress drop and rupture initiation point are the most important input parameters since these have a large effect on the ground shaking level at frequencies of engineering interest.
- Even though the level, distribution and spectral values of the ground motions differ significantly, the response spectra are consistent, showing the usefulness of ground motion modeling in estimating a realistic hazard for Istanbul and hence in risk mitigation efforts despite the large uncertainties involved.

Our efforts in the future should focus on understanding the accuracy of the most critical parameters influencing the ground motion, namely the rise time, rupture velocity, rupture initiation point and the stress drop.

### **Acknowledgements**

We thank all RELIEF partners for their contributions in the preparation of the input data to the seismic hazard analyses. We are grateful to Nelson Pulido for his involvement in various parts of the ground motion simulations. Colleagues from the KOERI, Istanbul are thanked for the valuable discussions throughout the project.

## References

- Ambraseys, N.N. and Finkel, C.F (1995): The seismicity of Turkey and adjacent areas: A historical review 1500-1800, Eren Yayincilik ve Kitapcilik Ltd.Sti., Istanbul. 240p.
- Ambraseys, N. N., Simpson, K. A. and Bommer, J. J. (1996): Prediction of horizontal response spectra in Europe, *Earthquake Eng. Struct. Dyn.* 25, 371-400.
- Ambraseys, N.N. and Jackson, J.A., (2000): Seismicity of the Sea of Marmara (Turkey) since 1500, *Geophys. J. Int.*, 141, F1-F6.
- Atakan, K., Ojeda, A., Meghraoui, M., Barka, A.A., Erdik, M. and Bodare, A., (2002): Seismic Hazard in Istanbul following the 17 August 1999 Izmit and 12 November 1999 Düzce Earthquakes, *Bulletin of the Seismological Society of America*, 92, 466-482.
- Aydinoglu, M.N., (1998): Specification for Structures to be Built in Disaster Areas, Part III – Earthquake Disaster Prevention, Ministry of Public Works and Settlement, Government of Republic of Turkey, Official Gazette, No. 23390.
- Barka, A., Akyüz, H.S., Altunel, E., Sunal, G., Cakir, Z., Dikbas, A., Yerli, B., Armijo, R., Meyer, B., de Chabaliere, J.B., Rockwell, T., Dolan, J.R., Hartleb, R. Dawson, T., Christofferson, S., Tucker, A., Fumal, T., Langridge, R., Stenner, H., Lettis, W., Bachhuber, J. and Page, W. (2002): The Surface Rupture and Slip Distribution of the 17 August 1999 Izmit Earthquake (M 7.4), North Anatolian Fault, *Bulletin of the Seismological Society of America*, 92, 1, 43-60.
- Bender, B. and D.M. Perkins (1987): SEISRISK III: A computer program for seismic hazard estimation. United States geological Survey, Bulletin, 1772, 24p.
- Birgören, G., Özel, O., Fahjan, Y. and Erdik, M., (2004): Determination of site effects in Istanbul area using a small earthquake record of the dense strong motion network, XXIX General Assembly of the European Seismological Commission, Potsdam, Germany, poster no. 249.
- Boore, D. M. (1983): Stochastic simulation of high frequency ground motions based on seismological models of the radiated spectra, *Bull. Seism. Soc. Am.*, 73, 1865-1894.
- Boore, D. M., Joyner, W. B. and Fumal, T. E. (1997): Equations for estimating horizontal response spectra and peak accelerations from western North American earthquakes: a summary of recent work, *Seismological Research Letters*, 68, 1, 128-153.
- Bouchon, M. (1981): A simple method to calculate Green's functions for elastic layered media, *Bull. Seism. Soc. Am.*, 71, 959-971.
- Brune, J., (1970): Tectonic stress and the spectra of seismic shear waves from earthquakes. *J. Geophys. Res.*, 75, 4997-5009.
- Campbell, K. W. (1997): Empirical near source attenuation relationship for horizontal and vertical components of peak ground acceleration, peak ground velocity, and pseudo absolute acceleration response spectra, *Seismological Research Letters*, 68, 1, 154-179.
- Cartwright, D. E. and Longuet-Higgins, M. S. (1956): The statistical distribution of the maxima of a random function, *Proc. R. Soc. London*, A237, 212-232.
- Cornell, C.A. (1968): Engineering seismic risk analysis. *Bull. Seism. Soc. Am.*, 58, 1583-1606.
- Das, S. and Kostrov, B.V., (1986): Fracture of a single asperity on a finite fault: a model for weak earthquakes? In: Das, S., Boatwright, J., Scholz, C. (Eds.). *Earthquake source mechanism*. American Geophysical Union, Washington, pp.91-96.
- Erdik, M., Alpay Biro, Y., Onur, T., Sesetyan, K. and Birgören, G. (1999): Assessment of earthquake hazard in Turkey and neighbouring regions. *Annali di Geofisica*, Vol.42, N0.6, 1125-1138.
- Erdik, M., Demircioglu, M., Sesetyan, K., Durukal, E. And Siyahi, B., (2004): Earthquake hazard in Marmara Region, Turkey, *Soil Dynamics and Earthquake Engineering*, 24, 605-631.
- Eyidogan, H., Güçlü, U., Utku, Z. and Degirmenci, E (1991): Türkiye büyük depremleri makro-sismik rehberi (1900-1988) (in Turkish), Istanbul Technical University, Faculty of Mining, Department of Geological Engineering. Kurtis Matbaasi, Istanbul. 198p.
- Gurbuz, C., Aktar, M., Eyidogan, H., Cisternas, A., Haessler, H., Barka, A., Ergin, M., Turkelli, N., Polat, O., Ucer, S.B., Kuleli, S., Baris, S., Kaypak, B., Bekler, T., Zor, E., Bicmen, F., and Yoruk, A.,

- (2000): The seismotectonics of the Marmara region (Turkey): results from a microseismic experiment. *Tectonophysics*, 316, 1-17.
- Hubert-Ferrari, A., Barka, A., Jacques, E., Nalbant, S.S., Meyer, B., Armijo, R., Tapponnier, P. and King, G.C.P. (2000): Seismic hazard in the Marmara Sea region following the 17 August 1999 Izmit earthquake, *Nature*, 404, 269-273.
- Irikura, K. (1986): Prediction of strong acceleration motion using empirical Green's function, *Proceedings of the 7th Japan. Earthq. Eng. Symp.*, 151-156.
- Kuscu, I., Demirbas, E., Kurt, H., Ican, A.K., Güney, A.B., and Imren, C. (2000): The North Anatolian Fault Zone under the sea of Marmara, imaged by seismic reflection profiles. In: K. Okumura, K. Takada and H. Goto (Eds.). *Active Fault Research for the New Millennium*, Letter Press Co. Ltd., Hiroshima, Japan, 195-198.
- Malagnini, L. and Herrmann, R. B. (2000): Ground-Motion Scaling in the Region of the 1997 Umbria-Marche Earthquake (Italy), *Bulletin of the Seismological Society of America*, 90, 4, 1041-1051.
- Malagnini, L., Herrmann, R. B. and Koch, K. (2000): Regional Ground-Motion Scaling in Central Europe, *Bulletin of the Seismological Society of America*, 90, 4, 1052-1061.
- Malagnini, L., Herrmann, R. B. and Di Bona, M. (2000): Ground-Motion Scaling in the Apennines (Italy), *Bulletin of the Seismological Society of America*, 90, 4, 1062-1081.
- McGuire, R.K. (1976): EQRISK: Evaluation of earthquake risk to site. United States Geological Survey, Open File Report, 76-67, 69p.
- McGuire, R.K. (1993): Computations of seismic hazard. *Annali di Geofisica*, Vol. XXXVI, No.3-4, 181-200.
- Okay, A.I., Kaslilar-Özcan, A., Imren, C., Boztepe-Güney, A., Demirbag, E. and Kuscu, I., (2000): Active faults and evolving strike-slip basins in the Marmara Sea, northwest Turkey: a multichannel seismic reflection study, *Tectonophysics*, 321, 189-218.
- Ordaz, M (1999): CRISIS99. A computer program to compute seismic hazard. Autonomous University of Mexico (UNAM).
- Parsons, T., Toda, S., Stein, R.S., Barka, A. and Dietrics, J.H., (2000): Heightened Odds of Large Earthquakes Near Istanbul: An interaction-Based Probability Calculation, *Science*, 288, 661-665.
- Parsons, T., (2004): Recalculated probability of  $M \geq 7$  earthquakes beneath the Sea of Marmara, Turkey, *Journal of Geophysical Research*, 109, B05304, doi: 10.1029/2003JB002667.
- Pulido, N. and Kubo, T. (2004): Near-fault strong motion complexity of the 2000 Tottori earthquake (Japan) from a broadband source asperity model, *Tectonophysics*, 390, 177-192.
- Pulido, N., Ojeda, A., Atakan, K. and Kubo, T. (2004): Strong ground motion estimation in the Sea of Marmara region (Turkey) based on a scenario earthquake, *Tectonophysics*, 391, 357-374.
- Sadigh, K., Chang, C.-Y., Egan, J. A., Makdisi, F. and Youngs, R. R. (1997): Attenuation relationship for shallow crustal earthquakes based on California strong motion data. *Seismological Research Letters*, 68, 1, 180-189.
- Somerville, P., Irikura, K., Graves, R., Sawada, S., Wald, D., Abrahamson, N., Iwasaki, Y., Kagawa, T., Smith, N., and Kowada, A., (1999): Characterizing crustal earthquake slip models for the prediction of strong ground motion. *Seismol. Res. Lett.*, 70, 59-80.
- Straub, C., Kahle, H.-G., Schindler, C., (1997): GPS and geologic estimates of the tectonic activity in the Marmara region, NW Anatolia. *J. Geophys. Res.* 102, 27 587–27 601.
- Schwartz, D.P. and Coppersmith, K.J. (1984): Fault behaviour and characteristic earthquakes – Examples from the Wasatch and San Andreas Fault zones. *J. Geophys. Res.*, 89, 5681-5698.
- Sørensen, M.B., Oprsal, I., Bonnefoy-Claudet, S., Atakan, K., Mai, P.M., Pulido, N. and Yalciner, C. (2005): Local site effects in Ataköy, Istanbul, Turkey, due to a future large earthquake in the Marmara Sea, submitted to *Geophysical Journal International*, June 2005.
- Tezcan, S.S., Kaya, E., Bal, I.E. and Özdemir, Z., (2002): Seismic amplification at Avcilar, Istanbul, *Engineering Structures*, 24, 661-667.
- Youngs, R.R. and Coppersmith, K.J. (1985): Implications of fault slip rates and earthquake recurrence models to probabilistic seismic hazard estimates. *Bull. Seismol. Soc. Am.*, 75, 939-964.

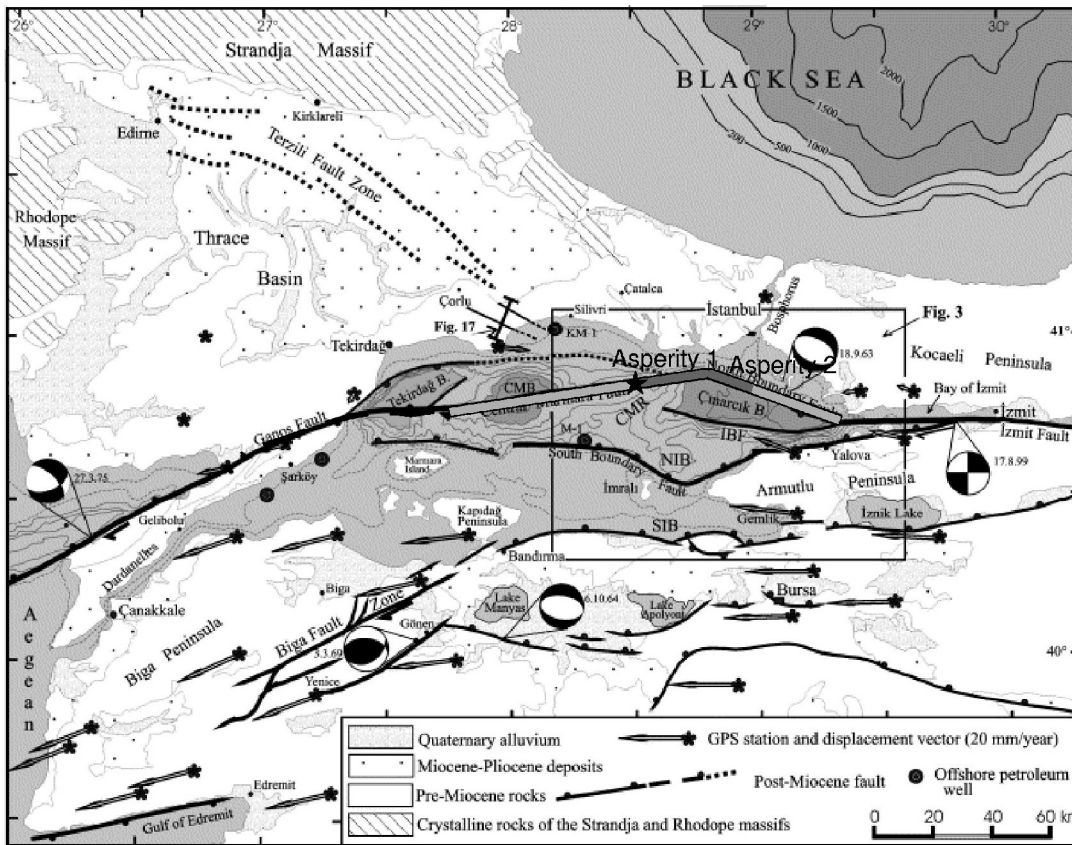


**Figure 1.1.** Map of active faulting in the Marmara Sea region (modified after Okay et al., 2000). The geometry of the standard scenario is given in the central Marmara Sea. The fault rupture is shown as a thick gray line, asperities are shown as darker gray line segments. The star shows the rupture initiation point.



Project No: EVG1-CT-2002-00069



Deliverable no. 26 (Partner # 6: UiB)

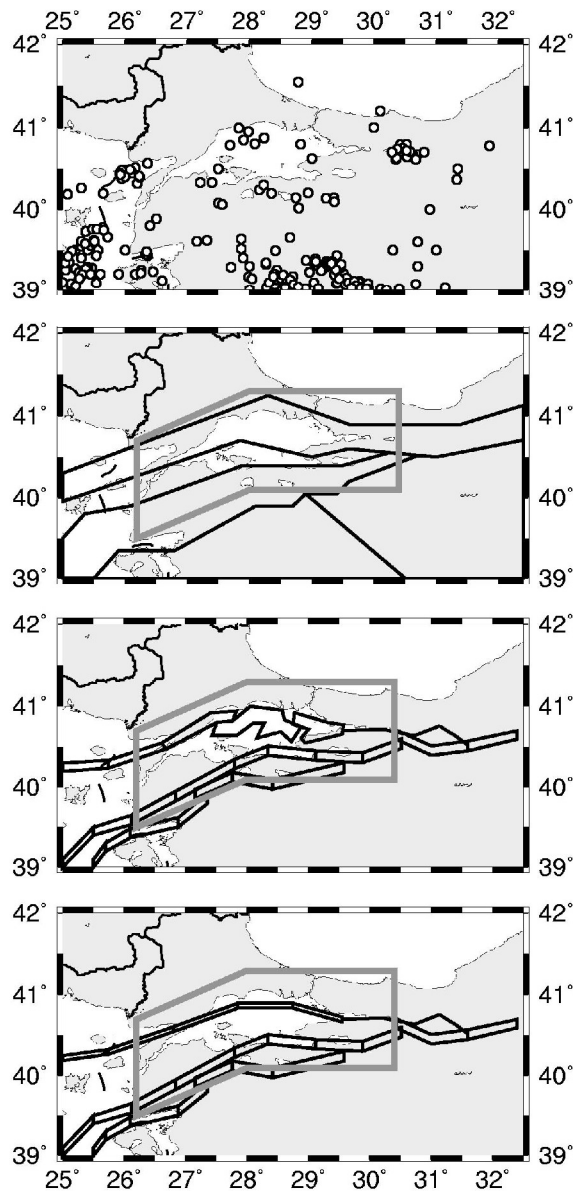


**Figure 2.1.1.** (a) Spatial distribution of the seismicity in the Marmara Region. The data are from the International Seismological Centre (ISC) database for the instrumental period. (b) The seismic source zonation for Model 1 (Poissonian area sources, similar to the one used in the recent GSHAP study by Erdik et al. (1999)). (c) The seismic sources used in Model 2 (faults as area zones, except for the Izmit and Düzce earthquakes, which are shown as line sources). (d) The seismic sources used in Model 3 (faults are shown as narrow area zones, except for the Izmit and Düzce earthquakes, which are shown as line sources).



Deliverable no. 26 (Partner # 6: UiB)



Project No: EVG1-CT-2002-00069

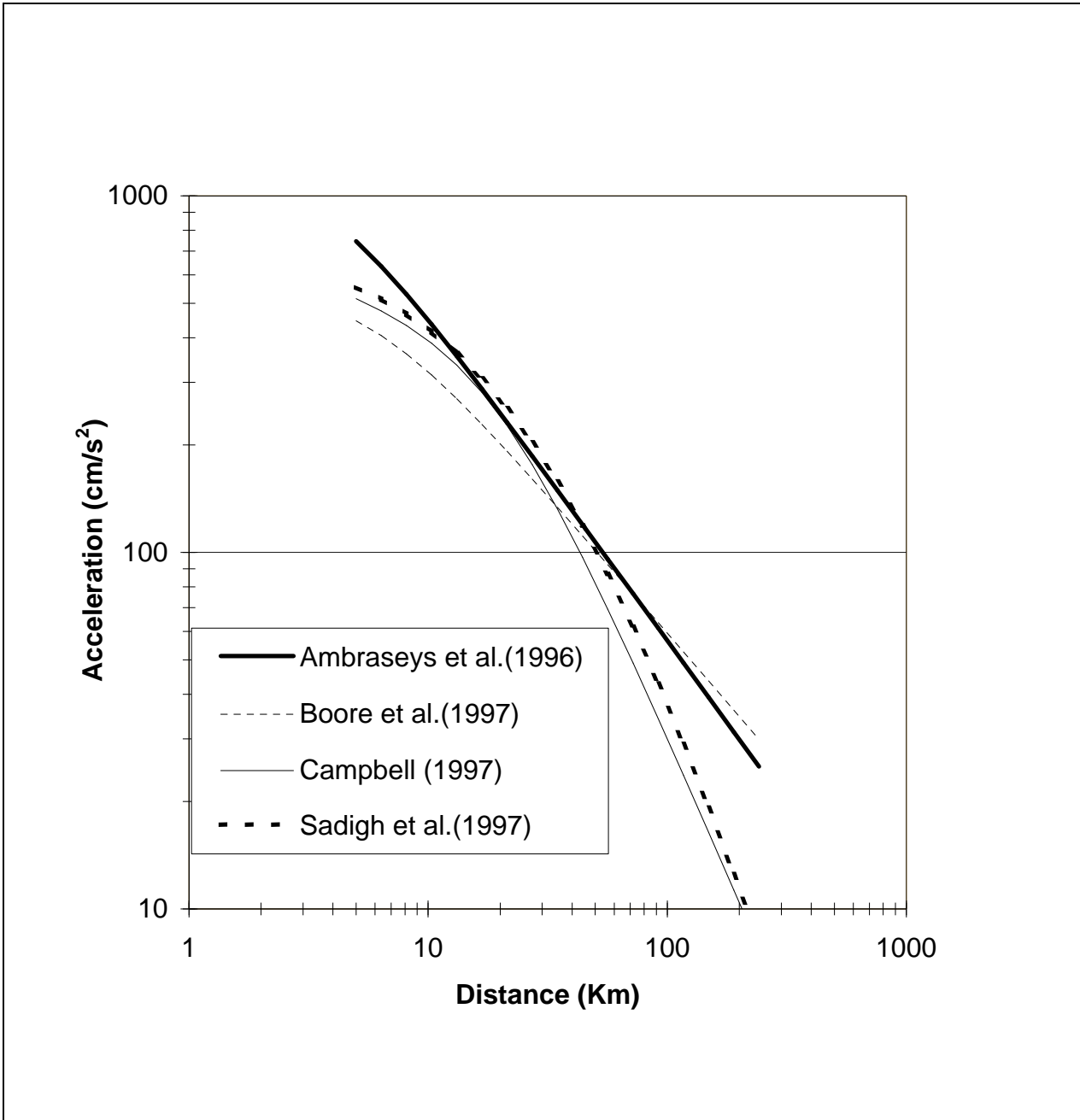


**Figure 2.1.2.** Diagram showing the four attenuation relations used in this study. The Ambraseys et al. (1996) relation is shown as thick solid line. Campbell (1997) is shown as thin solid line. Sadigh et al. (1997) is shown as the thick stippled line. Boore et al. (1997) is shown as thin stippled line.



**Project No: EVG1-CT-2002-00069**

**Deliverable no. 26 (Partner # 6: UiB)**

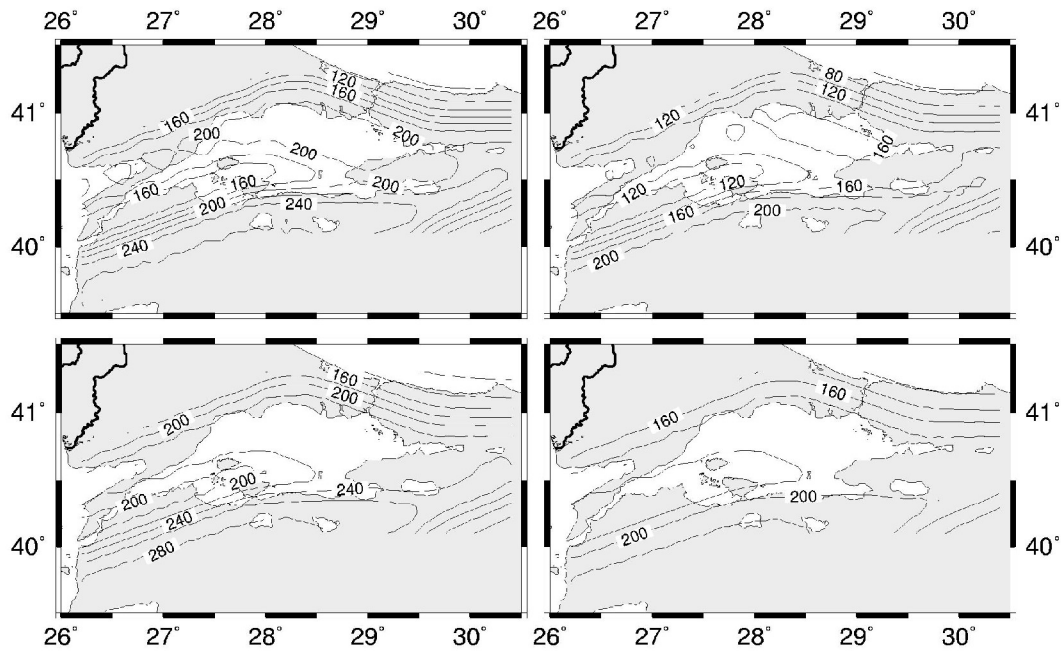


**Figure 3.1.1.** Distribution of PGA (in  $\text{cm/sec}^2$ ) using Model 1 (Poissonian) with the four different attenuation relations. Upper-left assume the Sadigh et al. (1997), relation. Lower-left assume the Ambraseys et al. (1997) relation. Upper-right assumes Campbell (1997). Lower-right assumes Boore et al. (1997). Note that the highest PGA values are obtained assuming the Ambraseys et al. (1996) relation.



Project No: EVG1-CT-2002-00069

Deliverable no. 26 (Partner # 6: UiB)

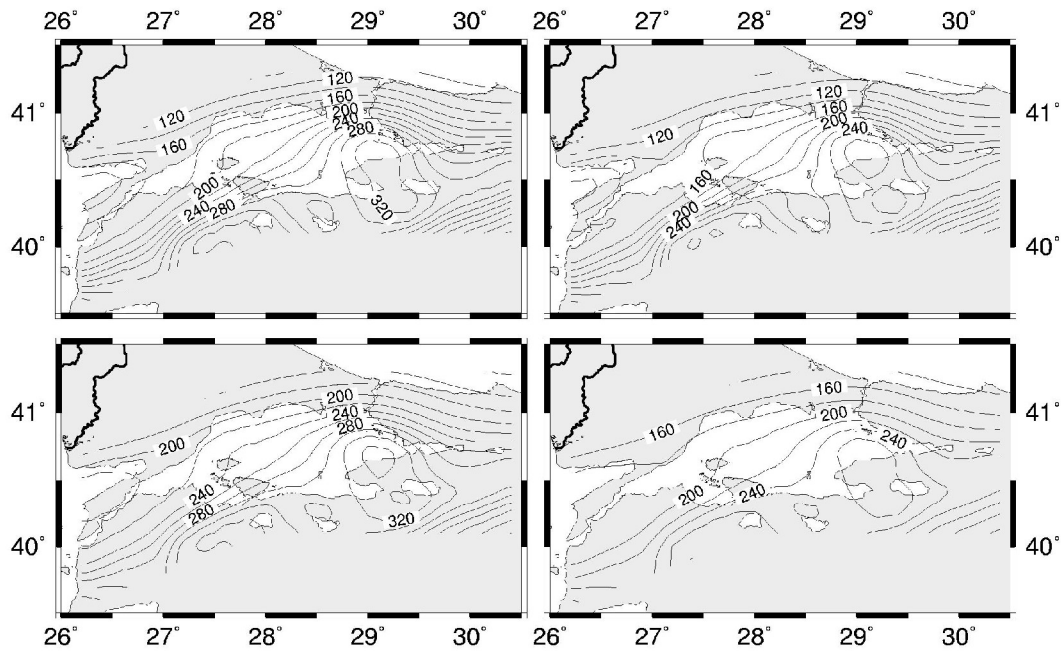


**Figure 3.1.2.** Distribution of the PGA (in  $\text{cm/sec}^2$ ) using Model 2 (Time dependent with gross zonation) with the four different attenuation relations. Upper-left is using Sadigh et al. (1997) relation. Lower-left is using Ambraseys et al. (1996) relation. Upper-right is using Campbell (1997). Lower-right is for Boore et al. (1997). Note that the highest PGA values are obtained when using the Ambraseys et al. (1996) relation.



Project No: EVG1-CT-2002-00069

Deliverable no. 26 (Partner # 6: UiB)

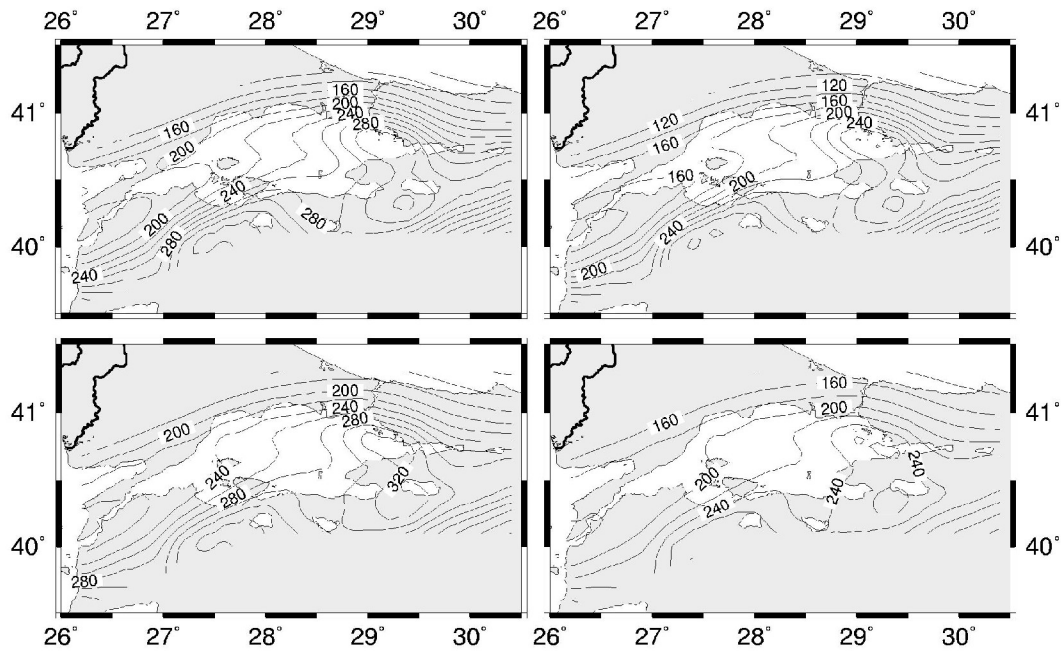


**Figure 3.1.3.** Distribution of the PGA (in  $\text{cm/sec}^2$ ) using Model 3 (Time dependent with fine zonation) with the four different attenuation relations. Upper-left is using Sadigh et al. (1997), relation. Lower-left is using Ambraseys et al. (1996) relation. Upper-right is using Campbell (1997). Lower-right is for Boore et al. (1997). Note that the highest PGA values are obtained when using the Ambraseys et al. (1996) relation.



Project No: EVG1-CT-2002-00069

Deliverable no. 26 (Partner # 6: UiB)

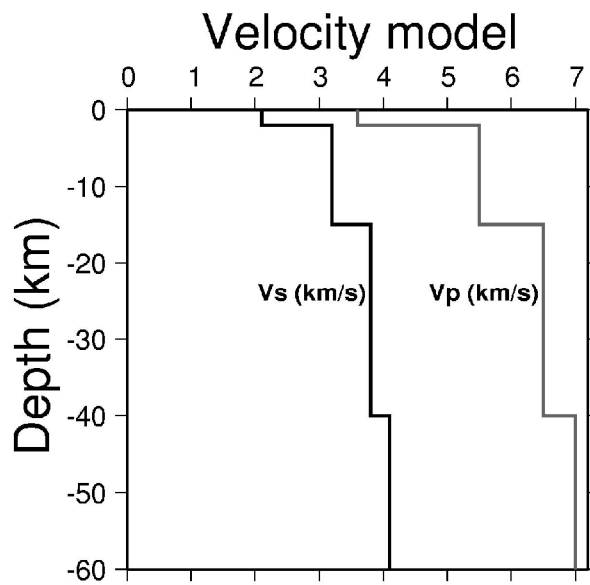


**Figure 3.2.1.** Velocity model for the Marmara Sea region (Serif Baris, personal communication, 2003).

Deliverable no. 26 (Partner # 6: UiB)



Project No: EVG1-CT-2002-00069

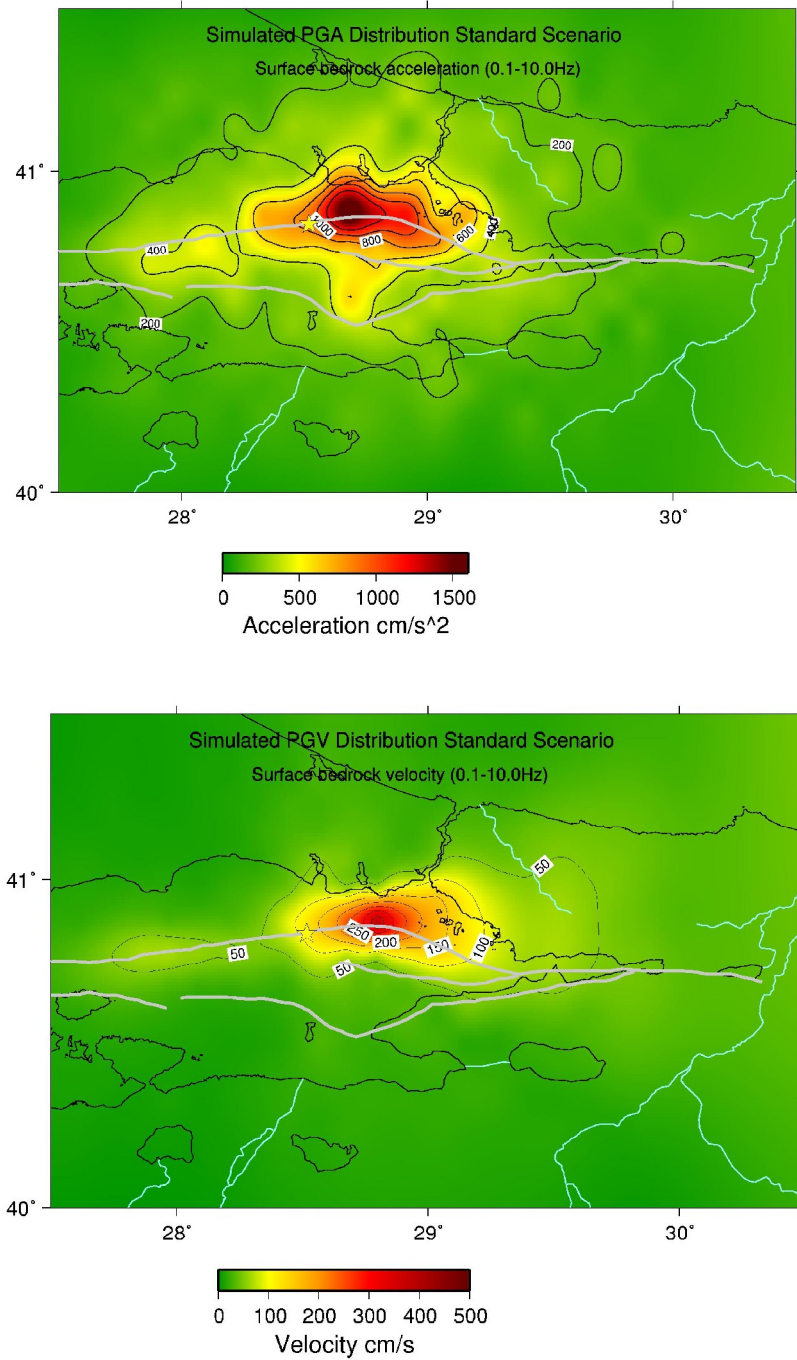


**Figure 3.2.2.** Simulation result for the standard scenario. a) PGA distribution, b) PGV distribution. Major faults are shown as grey lines and the rupture initiation point as a star.



Project No: EVG1-CT-2002-00069

Deliverable no. 26 (Partner # 6: UiB)

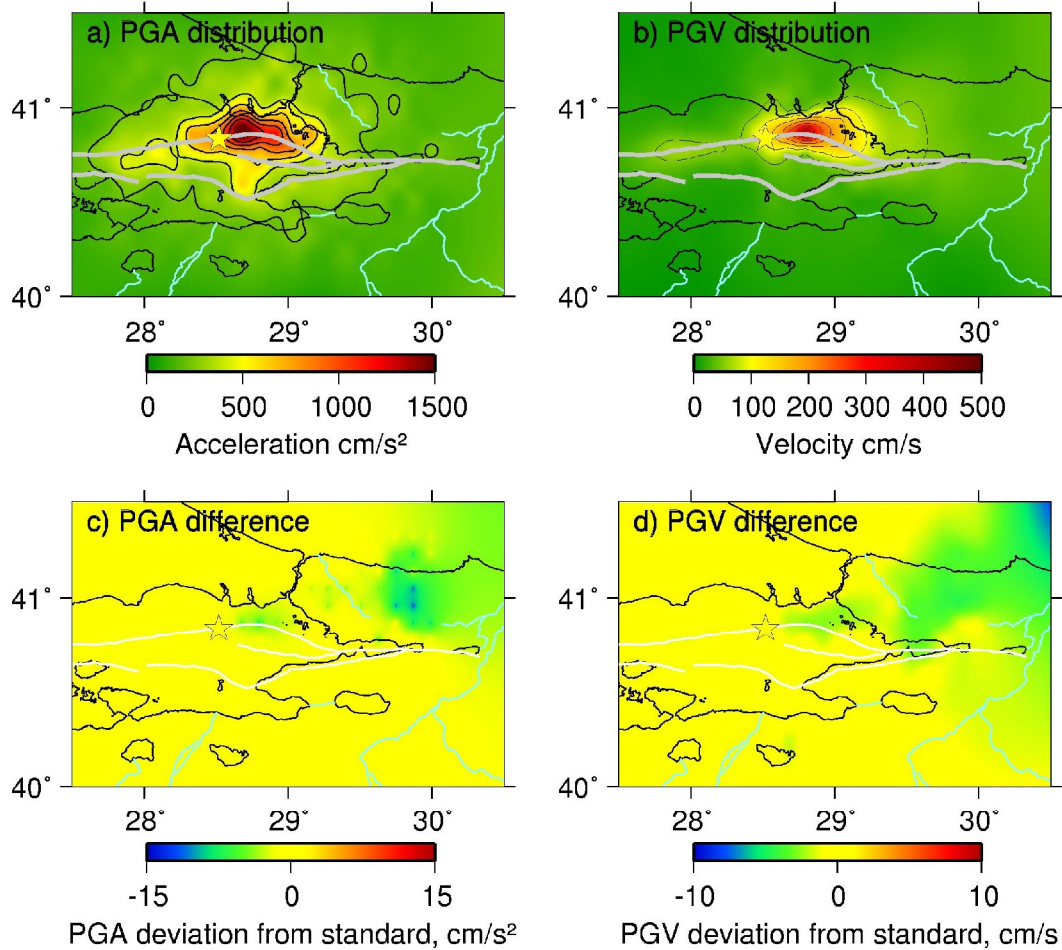


**Figure 3.2.3.** Simulation results for scenario 1a where the effect of low-frequency attenuation is tested. a) PGA distribution, b) PGV distribution, c) PGA difference between scenario 1a and standard scenario, d) PGV difference between scenario 1a and standard scenario. Major faults are shown as grey lines in a) and b) and as white lines in c) and d) and the rupture initiation point is shown as a star.



Deliverable no. 26 (Partner # 6: UiB)



Project No: EVG1-CT-2002-00069

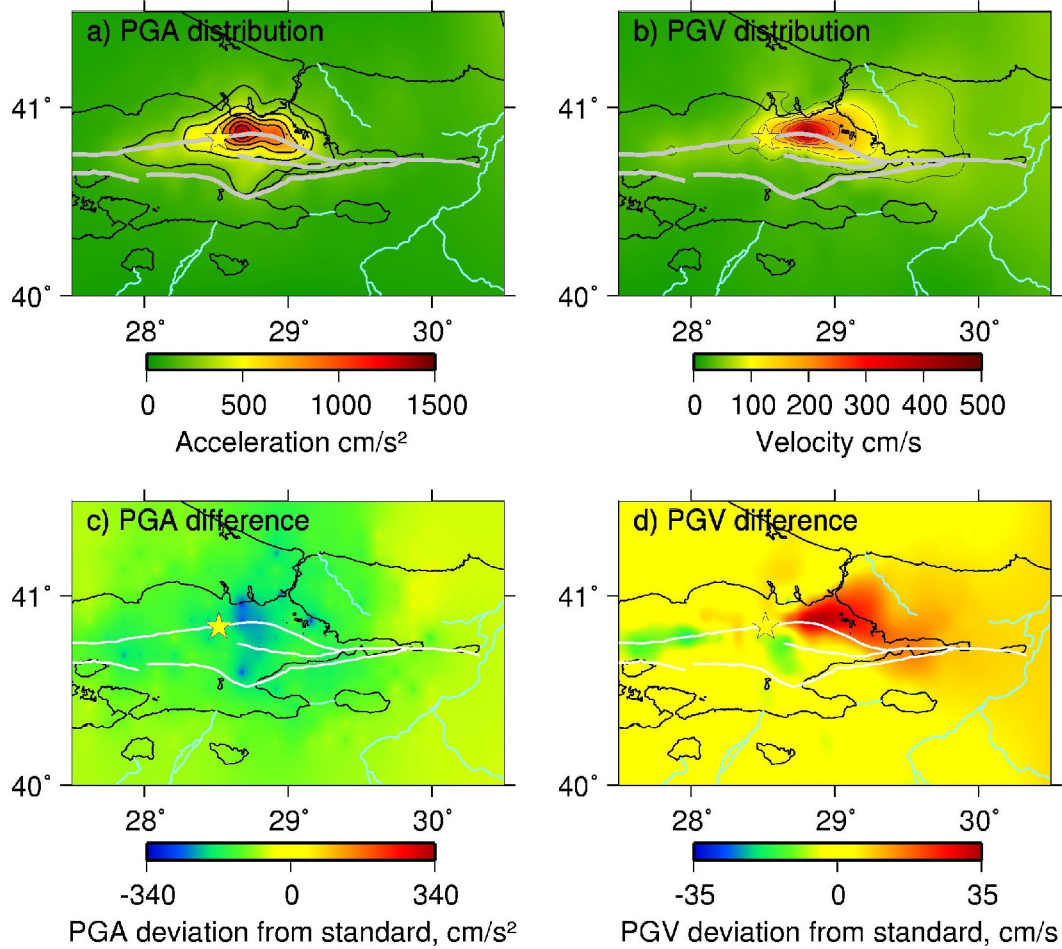


**Figure 3.2.4.** Simulation results for scenario 1b where the effect of high frequency attenuation is tested by lowering  $a$  in the relation  $Q=Q_0 \cdot f^a$ . a) PGA distribution, b) PGV distribution, c) PGA difference between scenario 1b and standard scenario, d) PGV difference between scenario 1b and standard scenario. Major faults are shown as grey lines in a) and b) and as white lines in c) and d) and the rupture initiation point is shown as a star.



Deliverable no. 26 (Partner # 6: UiB)



Project No: EVG1-CT-2002-00069

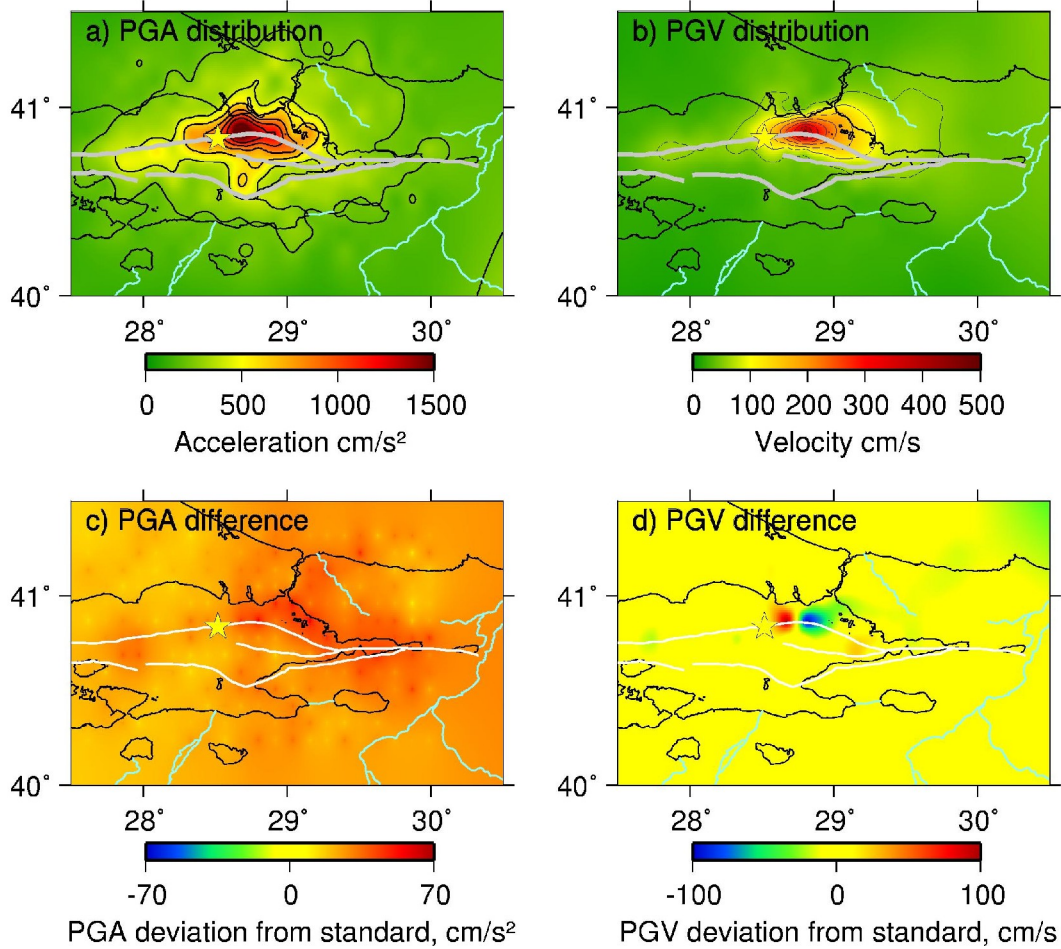


**Figure 3.2.5.** Simulation results for scenario 1c where the effect of high-frequency attenuation is tested by increasing  $Q_0$  in the relation  $Q=Q_0 \cdot f^{\alpha}$ . a) PGA distribution, b) PGV distribution, c) PGA difference between scenario 1c and standard scenario, d) PGV difference between scenario 1c and standard scenario. Major faults are shown as grey lines in a) and b) and as white lines in c) and d) and the rupture initiation point is shown as a star.



Project No: EVG1-CT-2002-00069

Deliverable no. 26 (Partner # 6: UiB)

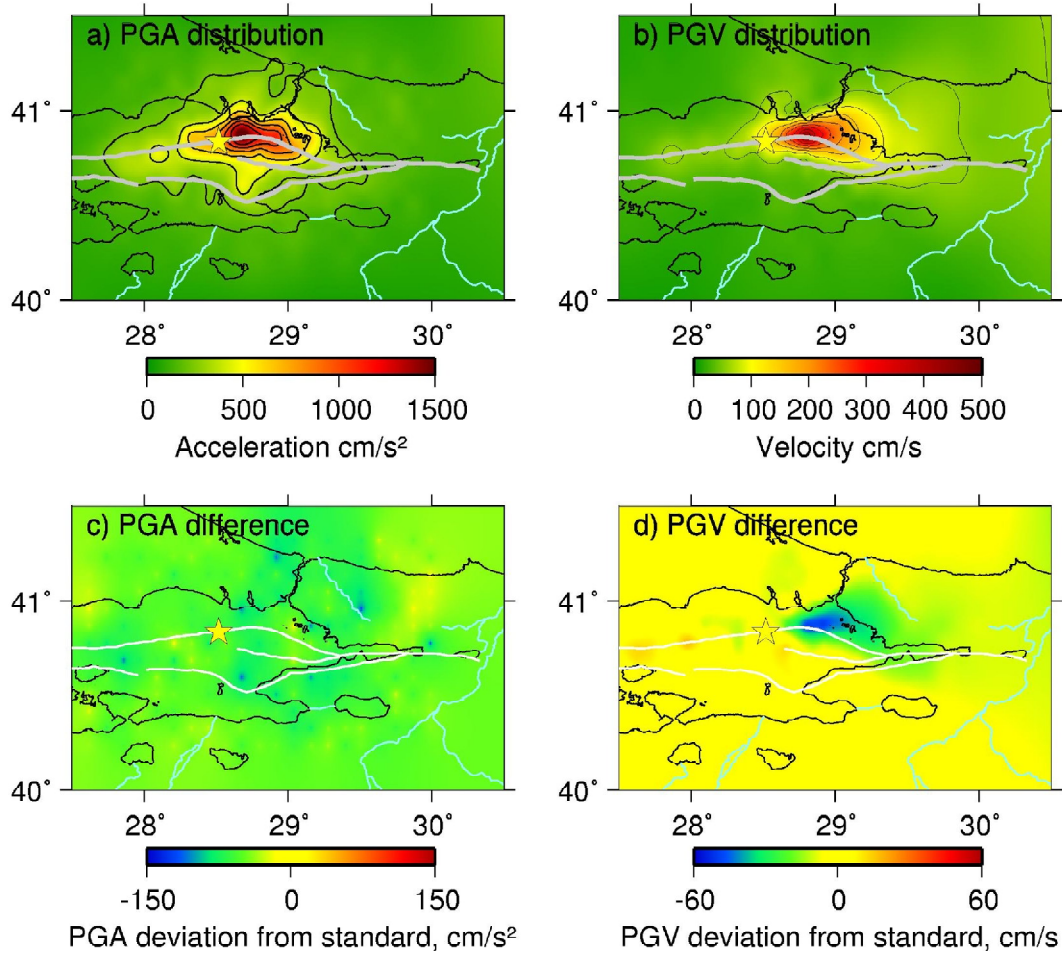


**Figure 3.2.6.** Simulation results for scenario 1d where the effect of high frequency attenuation is tested by lowering  $a$  and increasing  $Q_0$  in the relation  $Q=Q_0 \cdot f^a$ . a) PGA distribution, b) PGV distribution, c) PGA difference between scenario 1d and standard scenario, d) PGV difference between scenario 1d and standard scenario. Major faults are shown as grey lines in a) and b) and as white lines in c) and d) and the rupture initiation point is shown as a star.



Project No: EVG1-CT-2002-00069

Deliverable no. 26 (Partner # 6: UiB)

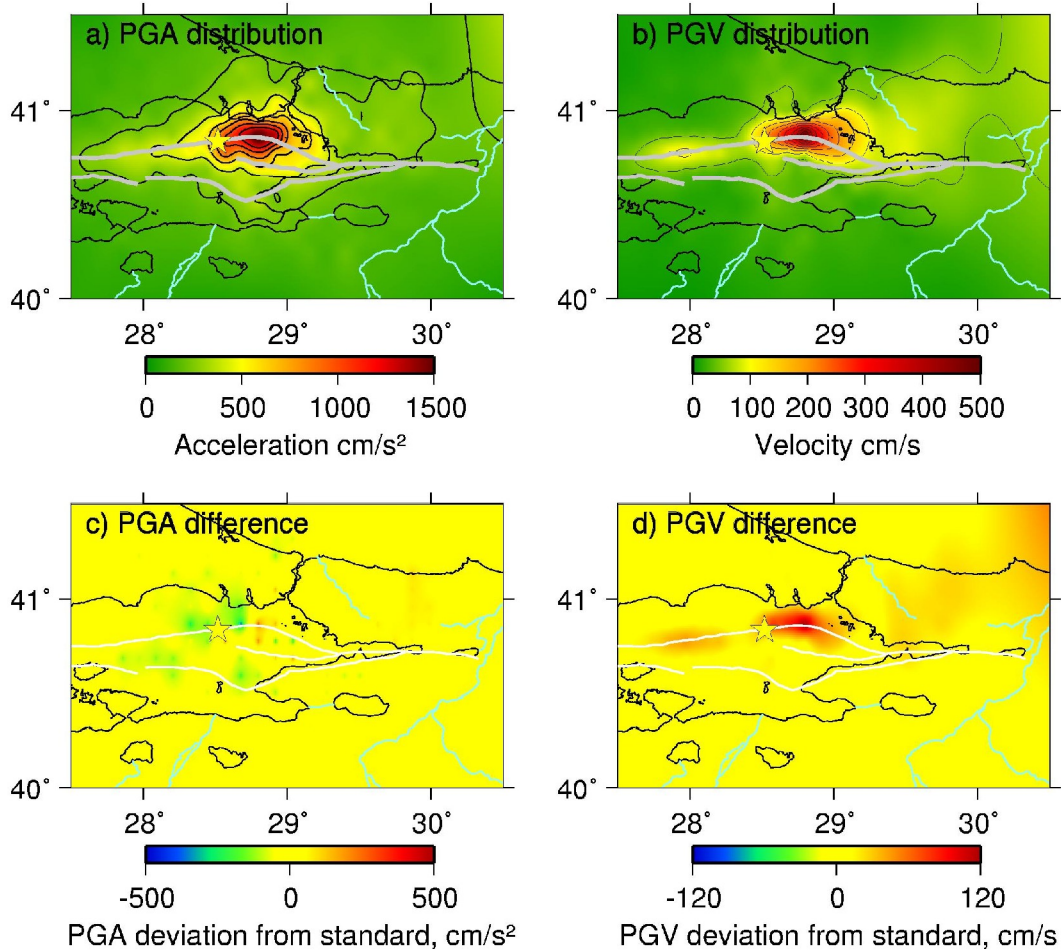


**Figure 3.2.7.** Simulation results for scenario 2a where the effect of a short rise time is tested. a) PGA distribution, b) PGV distribution, c) PGA difference between scenario 2a and standard scenario, d) PGV difference between scenario 2a and standard scenario. Major faults are shown as grey lines in a) and b) and as white lines in c) and d) and the rupture initiation point is shown as a star.



Project No: EVG1-CT-2002-00069

Deliverable no. 26 (Partner # 6: UiB)

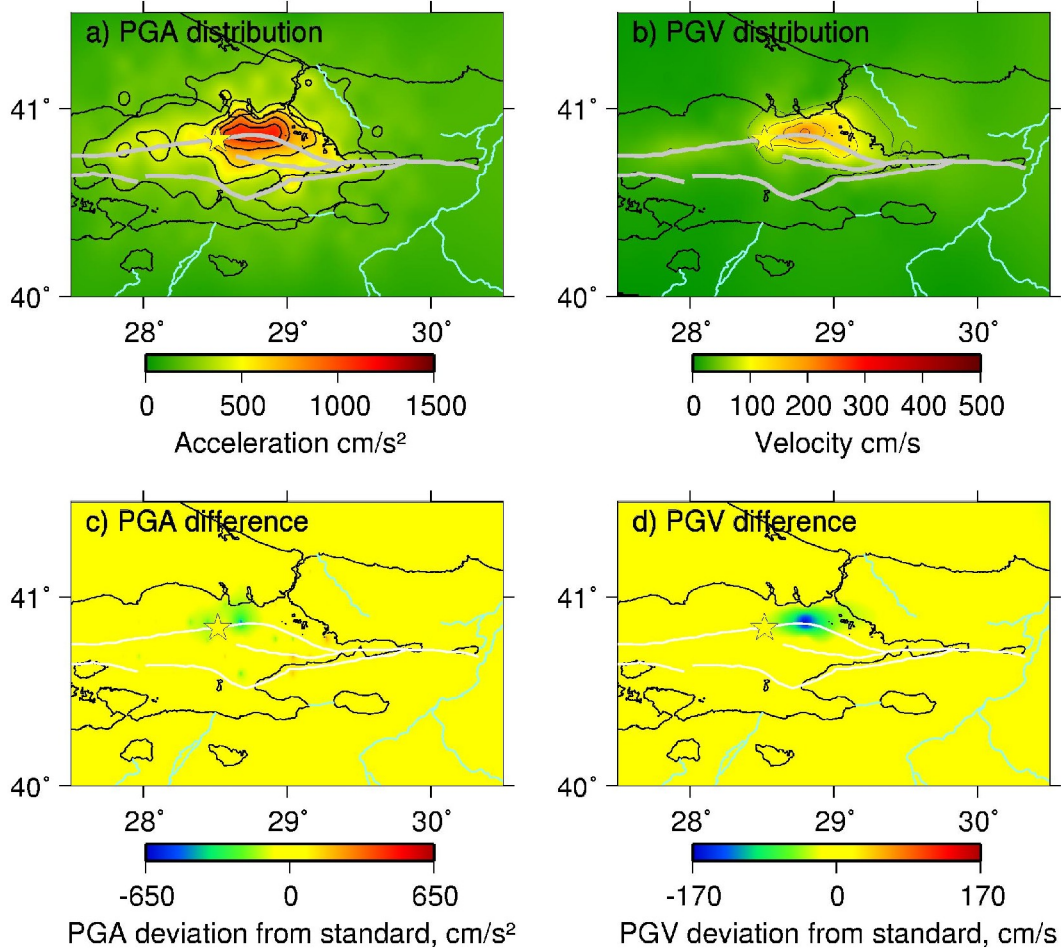


**Figure 3.2.8.** Simulation results for scenario 2b where the effect of a long rise time is tested. a) PGA distribution, b) PGV distribution, c) PGA difference between scenario 2b and standard scenario, d) PGV difference between scenario 2b and standard scenario. Major faults are shown as grey lines in a) and b) and as white lines in c) and d) and the rupture initiation point is shown as a star.



Project No: EVG1-CT-2002-00069

Deliverable no. 26 (Partner # 6: UiB)

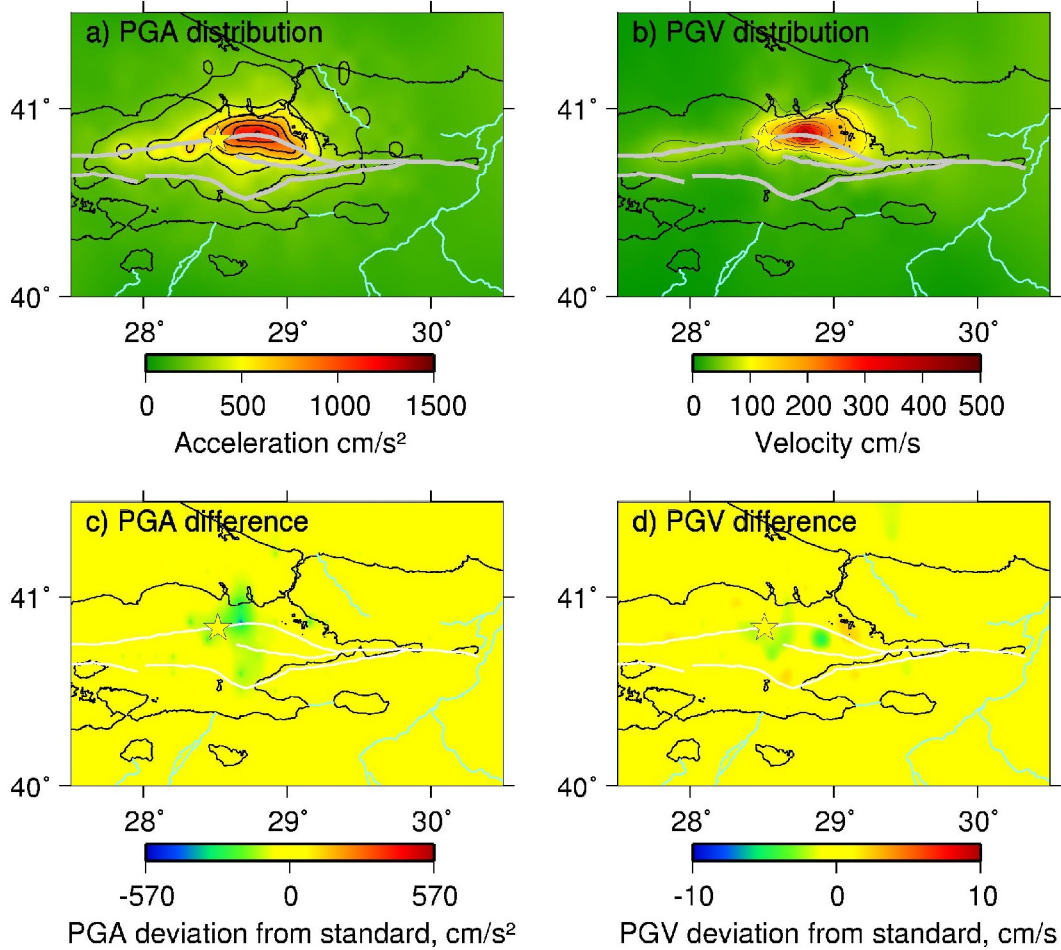


**Figure 3.2.9.** Simulation results for scenario 2c where the effect of a randomly varying rise time is tested. a) PGA distribution, b) PGV distribution, c) PGA difference between scenario 2c and standard scenario, d) PGV difference between scenario 2c and standard scenario. Major faults are shown as grey lines in a) and b) and as white lines in c) and d) and the rupture initiation point is shown as a star.



Deliverable no. 26 (Partner # 6: UiB)



Project No: EVG1-CT-2002-00069

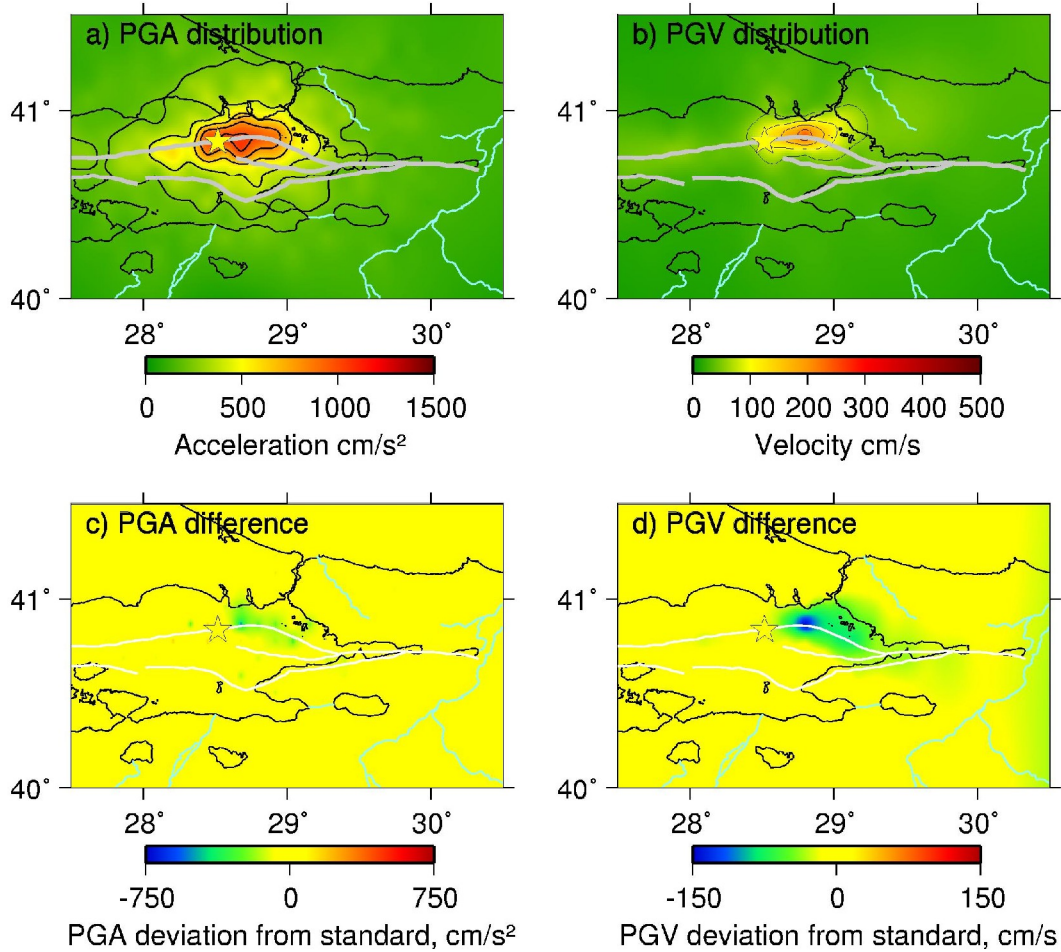


**Figure 3.2.10.** Simulation results for scenario 3a where the effect of a low rupture velocity is tested. a) PGA distribution, b) PGV distribution, c) PGA difference between scenario 3a and standard scenario, d) PGV difference between scenario 3a and standard scenario. Major faults are shown as grey lines in a) and b) and as white lines in c) and d) and the rupture initiation point is shown as a star.



Project No: EVG1-CT-2002-00069

Deliverable no. 26 (Partner # 6: UiB)

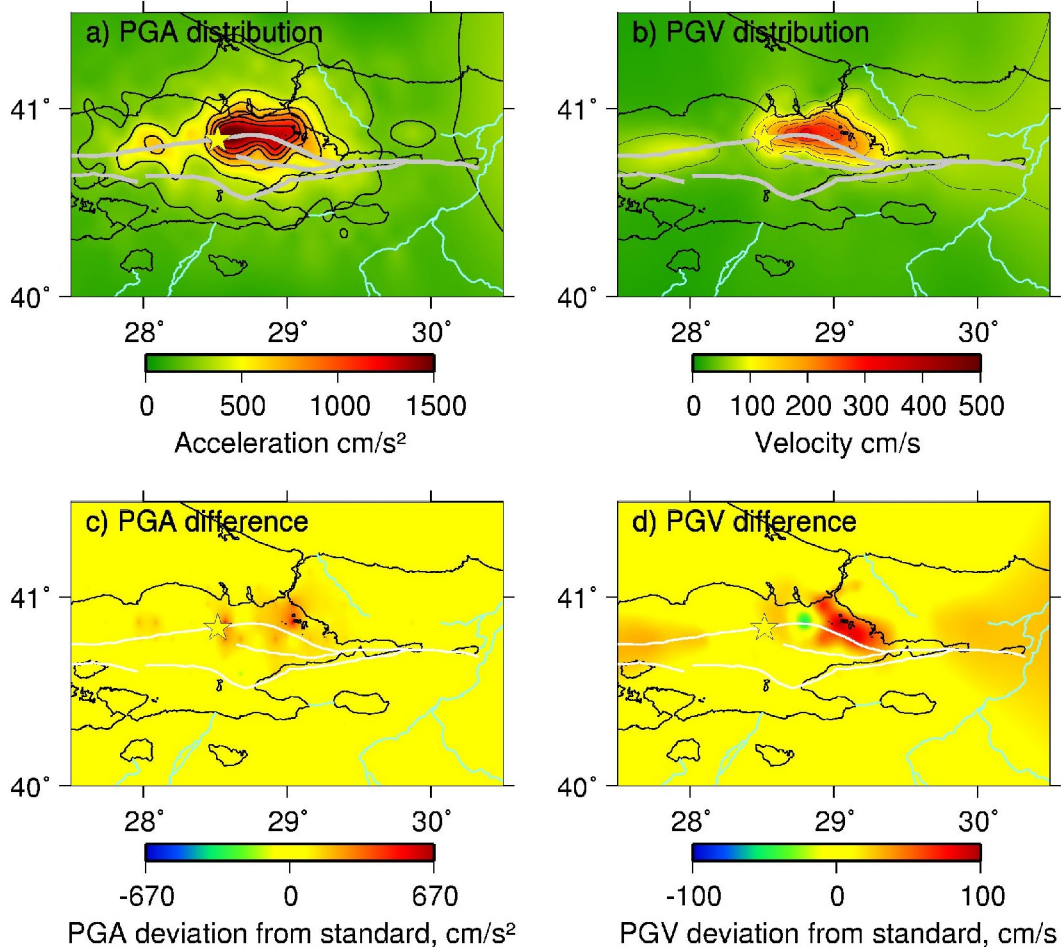


**Figure 3.2.11.** Simulation results for scenario 3b where the effect of a high rupture velocity is tested. a) PGA distribution, b) PGV distribution, c) PGA difference between scenario 3b and standard scenario, d) PGV difference between scenario 3b and standard scenario. Major faults are shown as grey lines in a) and b) and as white lines in c) and d) and the rupture initiation point is shown as a star.



Deliverable no. 26 (Partner # 6: UiB)



Project No: EVG1-CT-2002-00069

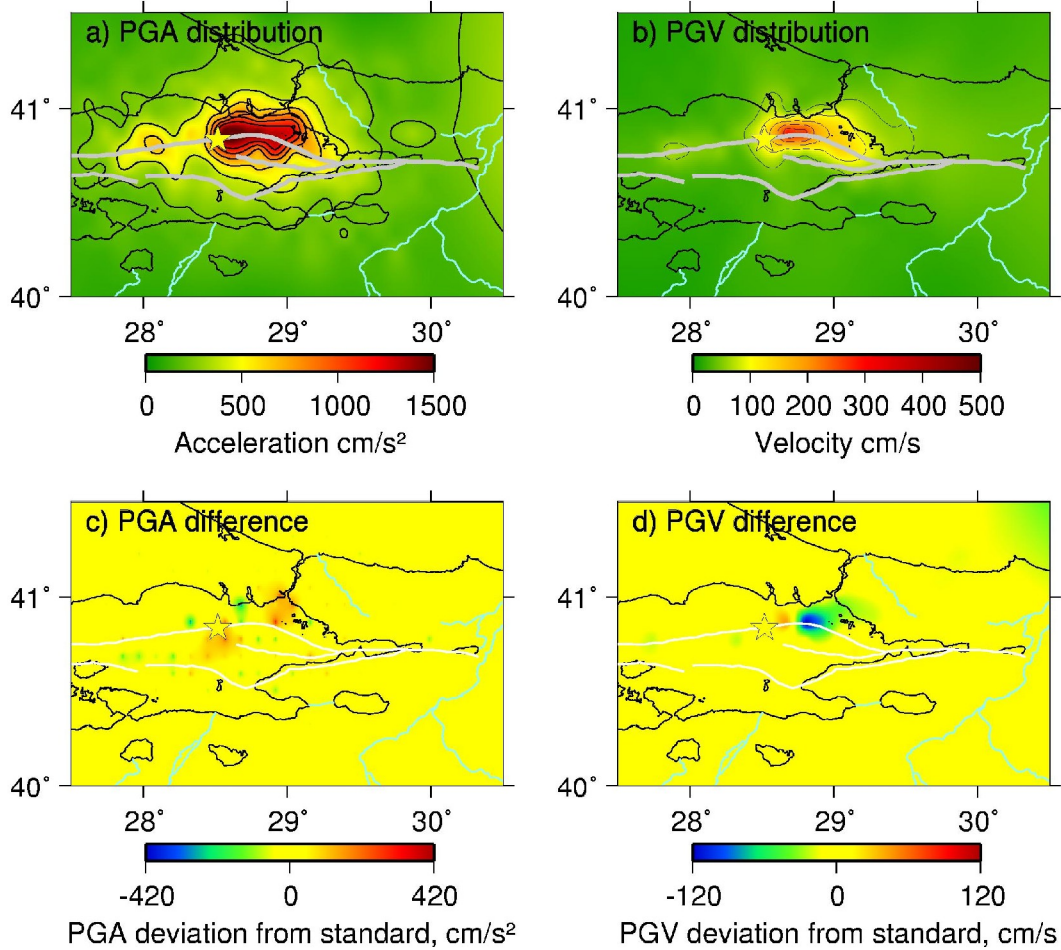


**Figure 3.2.12.** Simulation results for scenario 3c where the effect of a randomly varying rupture velocity is tested. a) PGA distribution, b) PGV distribution, c) PGA difference between scenario 3c and standard scenario, d) PGV difference between scenario 3c and standard scenario. Major faults are shown as grey lines in a) and b) and as white lines in c) and d) and the rupture initiation point is shown as a star.



Project No: EVG1-CT-2002-00069

Deliverable no. 26 (Partner # 6: UiB)

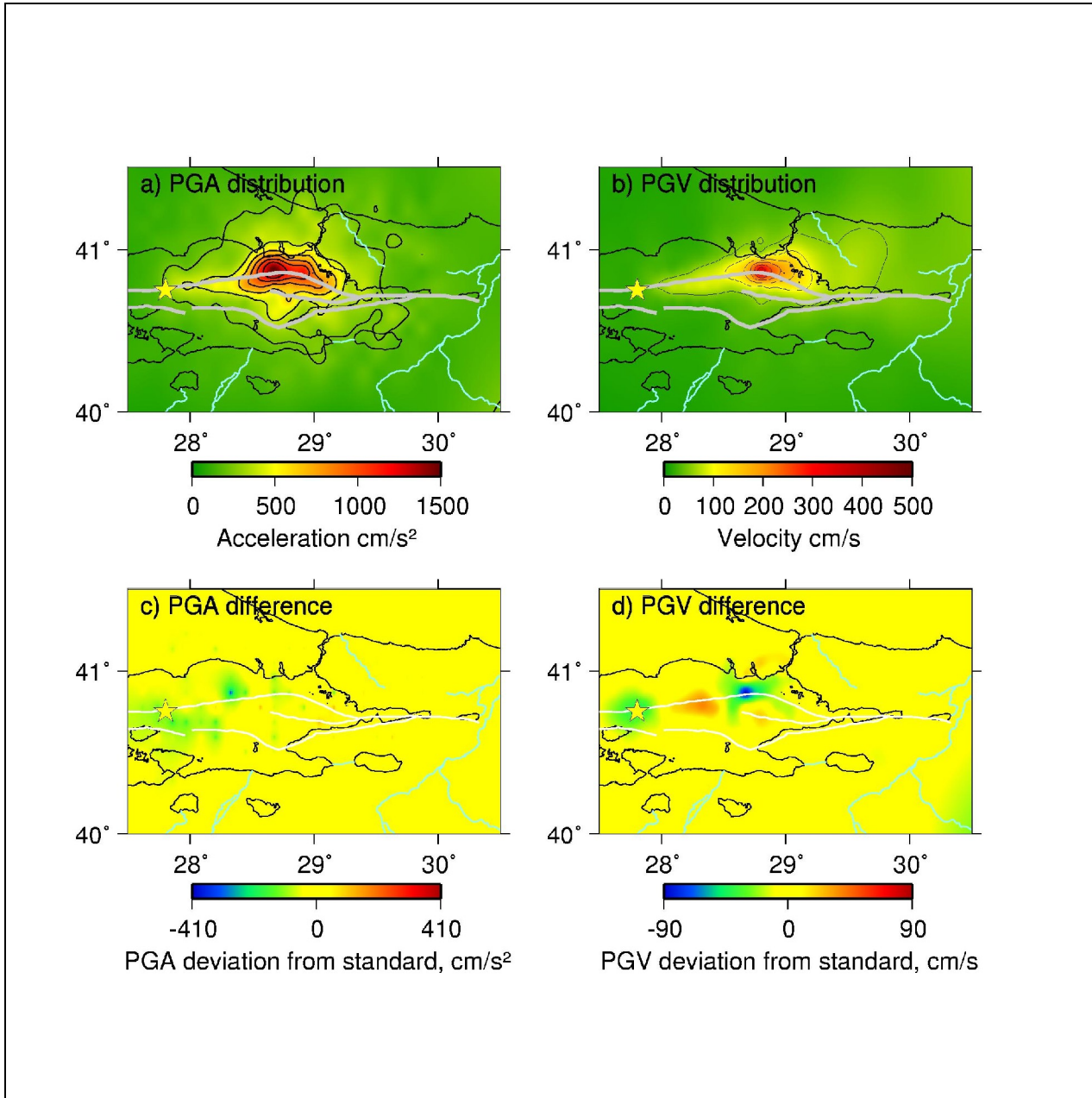


**Figure 3.2.13.** Simulation results for scenario 4a where the effect of rupture initiation point is tested. a) PGA distribution, b) PGV distribution, c) PGA difference between scenario 4a and standard scenario, d) PGV difference between scenario 4a and standard scenario. Major faults are shown as grey lines in a) and b) and as white lines in c) and d) and the rupture initiation point is shown as a star.



Project No: EVG1-CT-2002-00069

Deliverable no. 26 (Partner # 6: UiB)

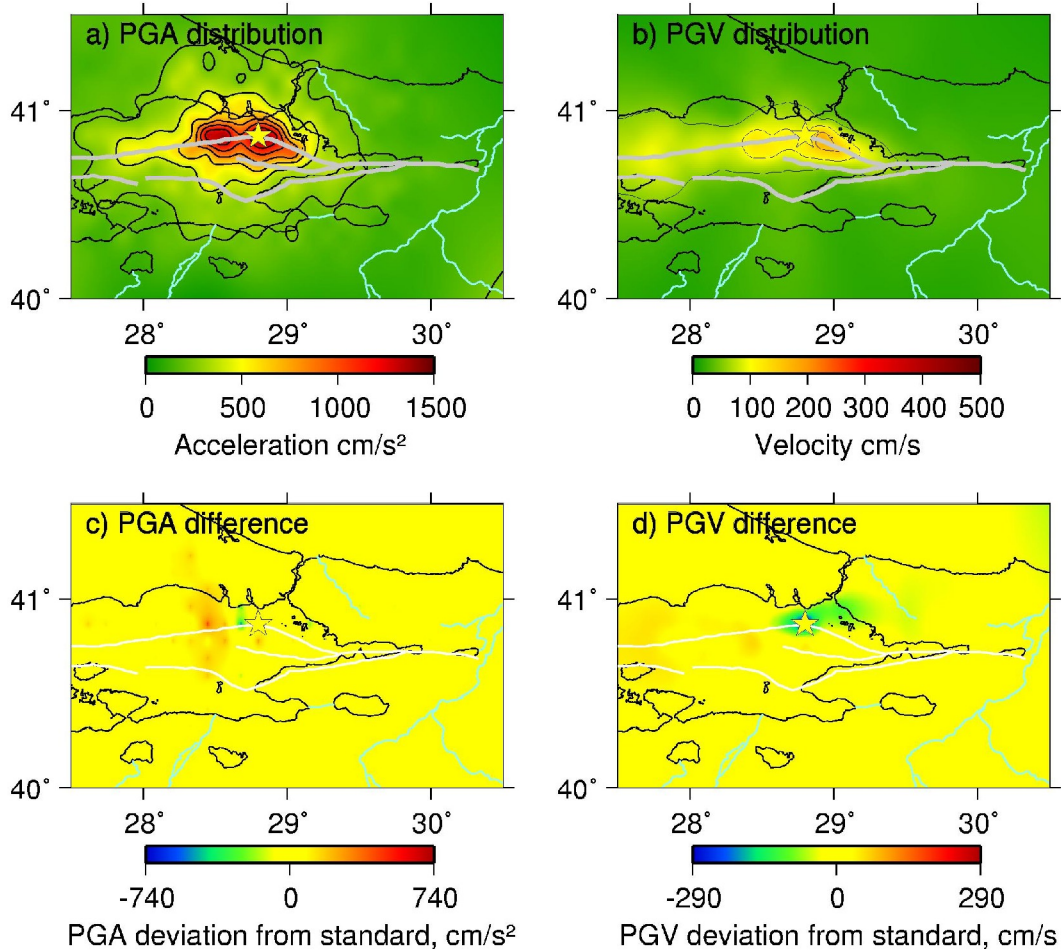


**Figure 3.2.14.** Simulation results for scenario 4b where the effect of rupture initiation point is tested. a) PGA distribution, b) PGV distribution, c) PGA difference between scenario 4b and standard scenario, d) PGV difference between scenario 4b and standard scenario. Major faults are shown as grey lines in a) and b) and as white lines in c) and d) and the rupture initiation point is shown as a star.



Project No: EVG1-CT-2002-00069

Deliverable no. 26 (Partner # 6: UiB)

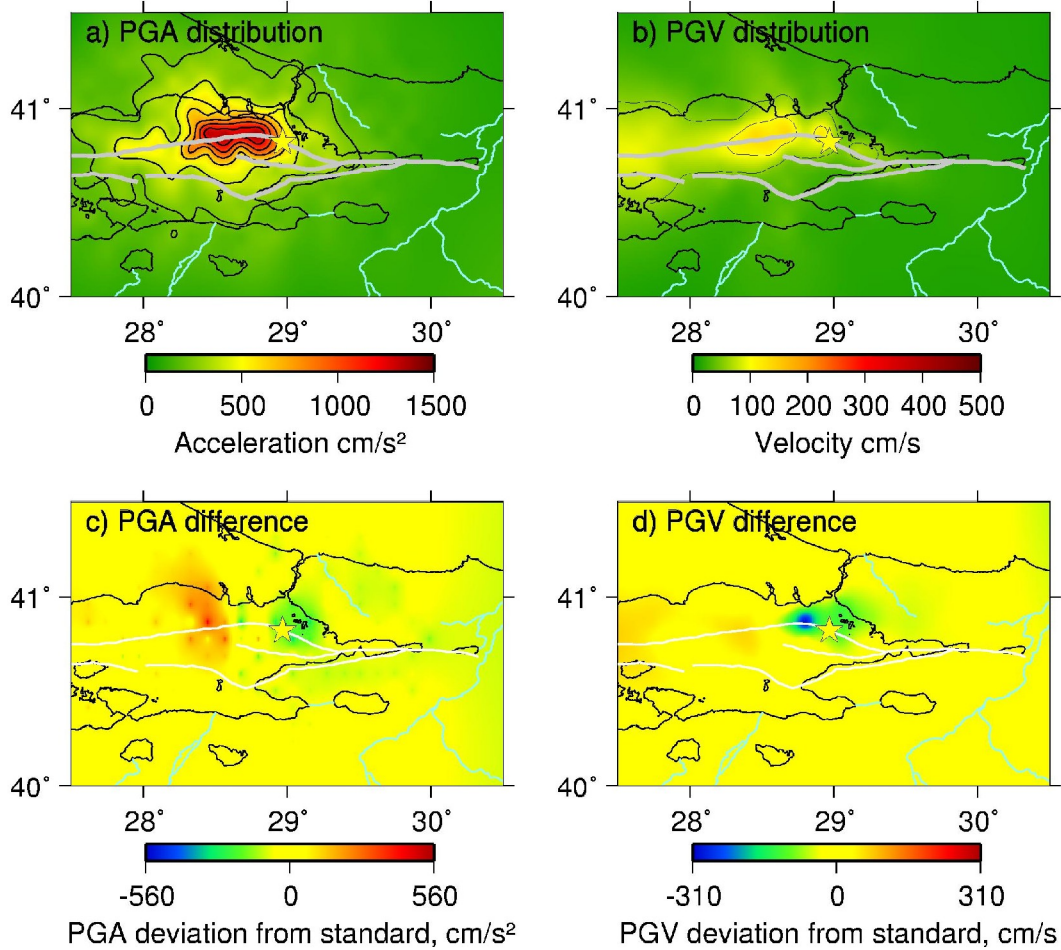


**Figure 3.2.15.** Simulation results for scenario 4c where the effect of rupture initiation point is tested. a) PGA distribution, b) PGV distribution, c) PGA difference between scenario 4c and standard scenario, d) PGV difference between scenario 4c and standard scenario. Major faults are shown as grey lines in a) and b) and as white lines in c) and d) and the rupture initiation point is shown as a star.



Project No: EVG1-CT-2002-00069

Deliverable no. 26 (Partner # 6: UiB)

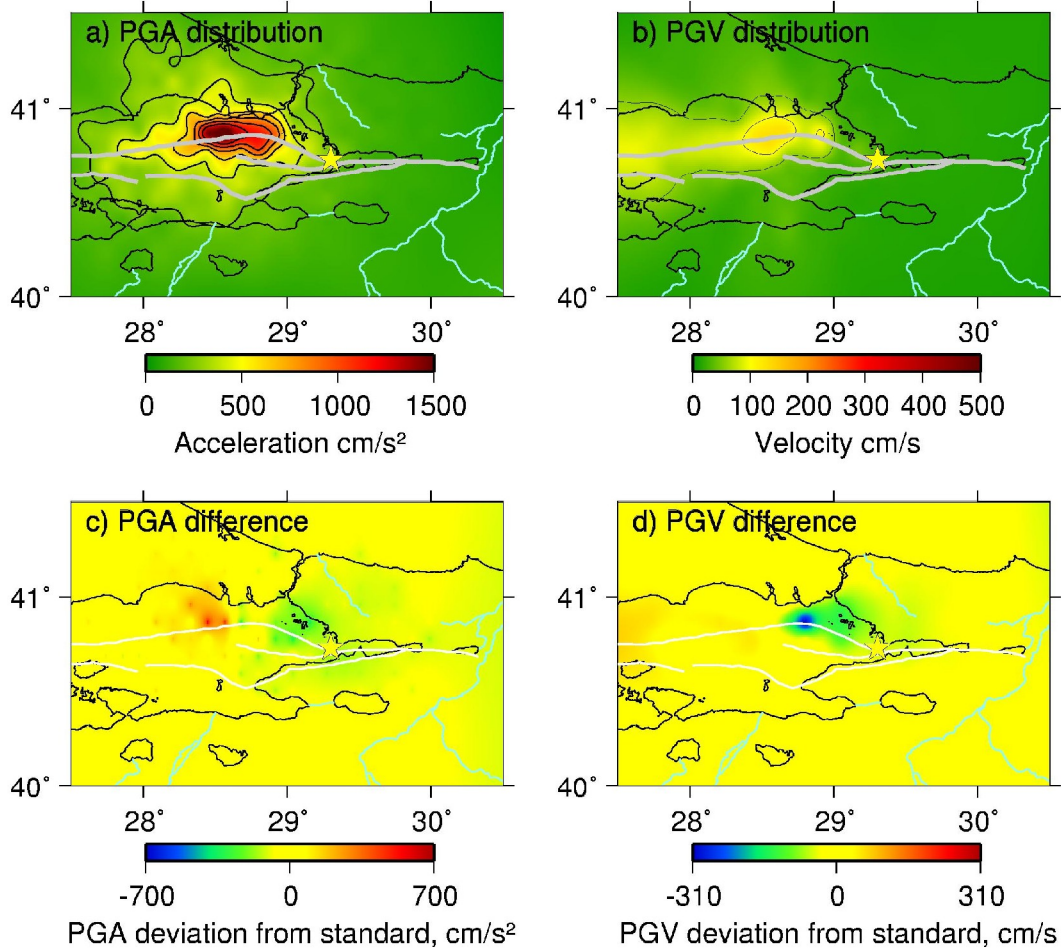


**Figure 3.2.16.** Simulation results for scenario 4d where the effect of rupture initiation point is tested. a) PGA distribution, b) PGV distribution, c) PGA difference between scenario 4d and standard scenario, d) PGV difference between scenario 4d and standard scenario. Major faults are shown as grey lines in a) and b) and as white lines in c) and d) and the rupture initiation point is shown as a star.



Project No: EVG1-CT-2002-00069

Deliverable no. 26 (Partner # 6: UiB)

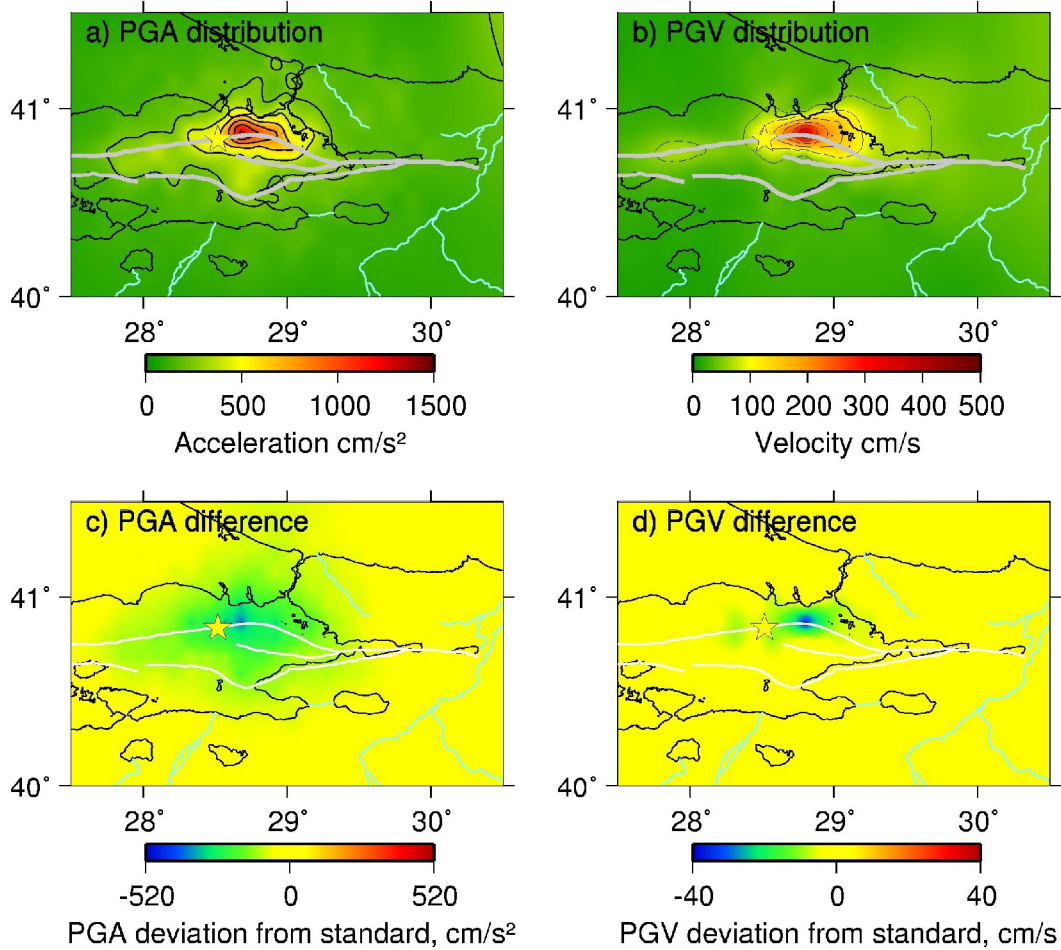


**Figure 3.2.17.** Simulation results for scenario 5a where the effect of low stress drop is tested. a) PGA distribution, b) PGV distribution, c) PGA difference between scenario 5a and standard scenario, d) PGV difference between scenario 5a and standard scenario. Major faults are shown as grey lines in a) and b) and as white lines in c) and d) and the rupture initiation point is shown as a star.



Deliverable no. 26 (Partner # 6: UiB)



Project No: EVG1-CT-2002-00069

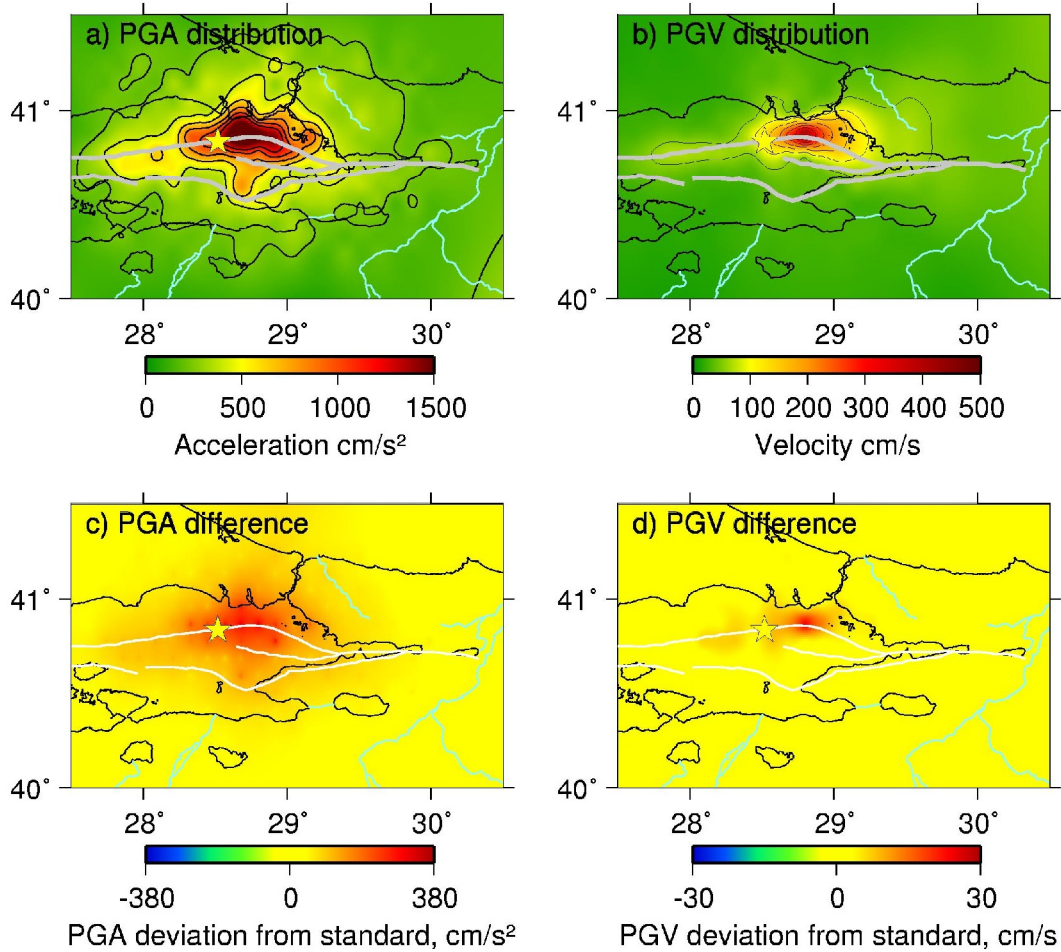


**Figure 3.2.18.** Simulation results for scenario 5b where the effect of high stress drop is tested. a) PGA distribution, b) PGV distribution, c) PGA difference between scenario 5b and standard scenario, d) PGV difference between scenario 5b and standard scenario. Major faults are shown as grey lines in a) and b) and as white lines in c) and d) and the rupture initiation point is shown as a star.



Deliverable no. 26 (Partner # 6: UiB)



Project No: EVG1-CT-2002-00069

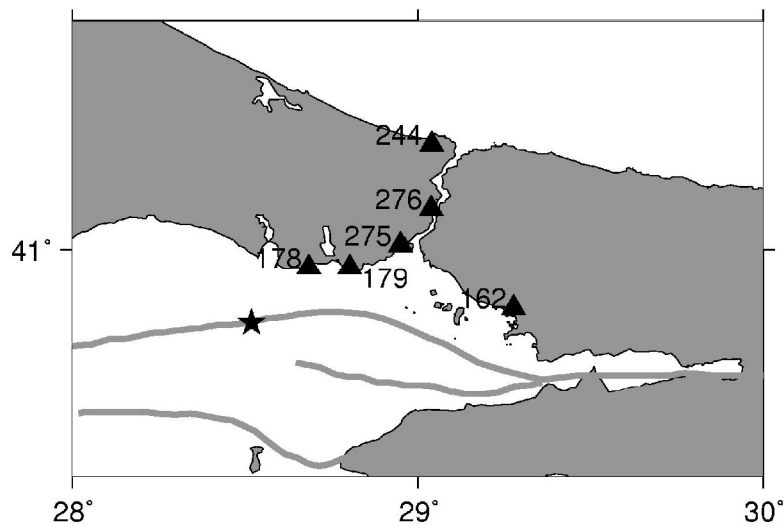


**Figure 3.2.19.** Location of the six sites analyzed in terms of spectral velocity and spectral acceleration. The numbers refer to the location of the six sites within the computational grid of 276 points. The grey lines show the location of the major faults in the area and the star shows the rupture initiation point for the standard scenario.



**Project No: EVG1-CT-2002-00069**

**Deliverable no. 26 (Partner # 6: UiB)**

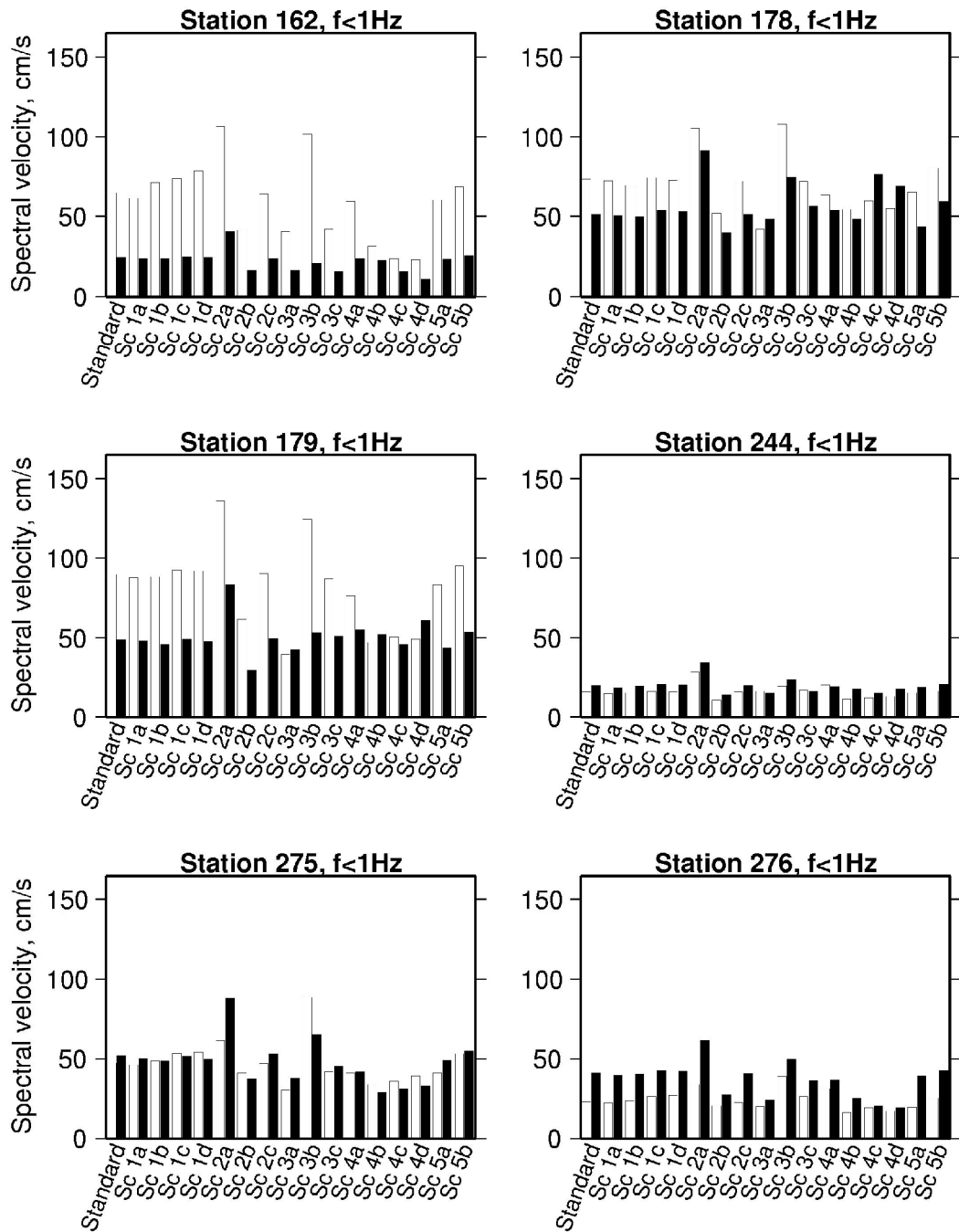


**Figure 3.2.20.** Spectral velocity at the sites in Figure 20 in the frequency band  $f < 1\text{Hz}$ . White bars represent the NS component of the ground motion and black bars represent the EW component.



Deliverable no. 26 (Partner # 6: UiB)



Project No: EVG1-CT-2002-00069

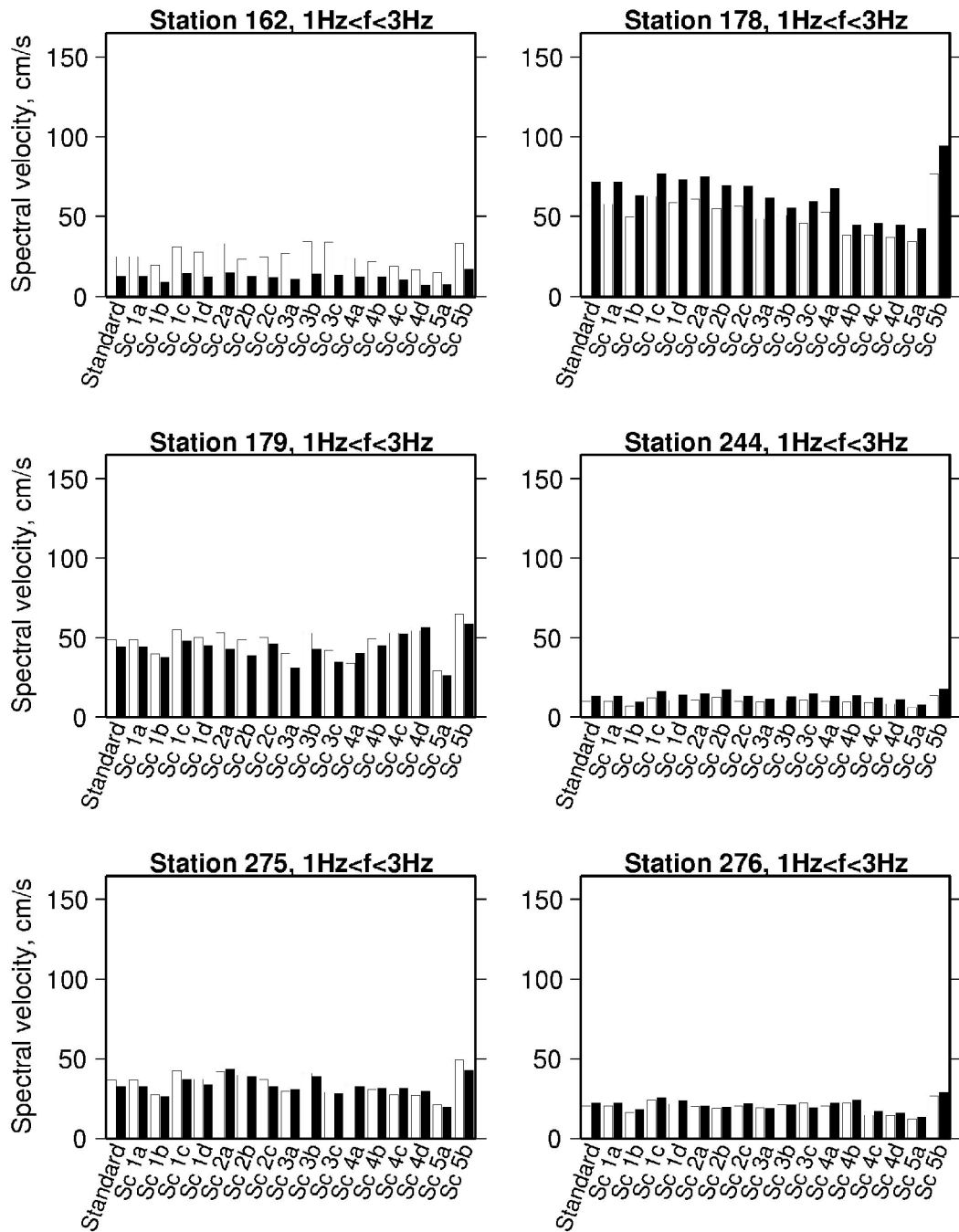


**Figure 3.2.21.** Spectral velocity at the sites in Figure 20 in the frequency band 1Hz < f < 3Hz. White bars represent the NS component of the ground motion and black bars represent the EW component.



Deliverable no. 26 (Partner # 6: UiB)



Project No: EVG1-CT-2002-00069

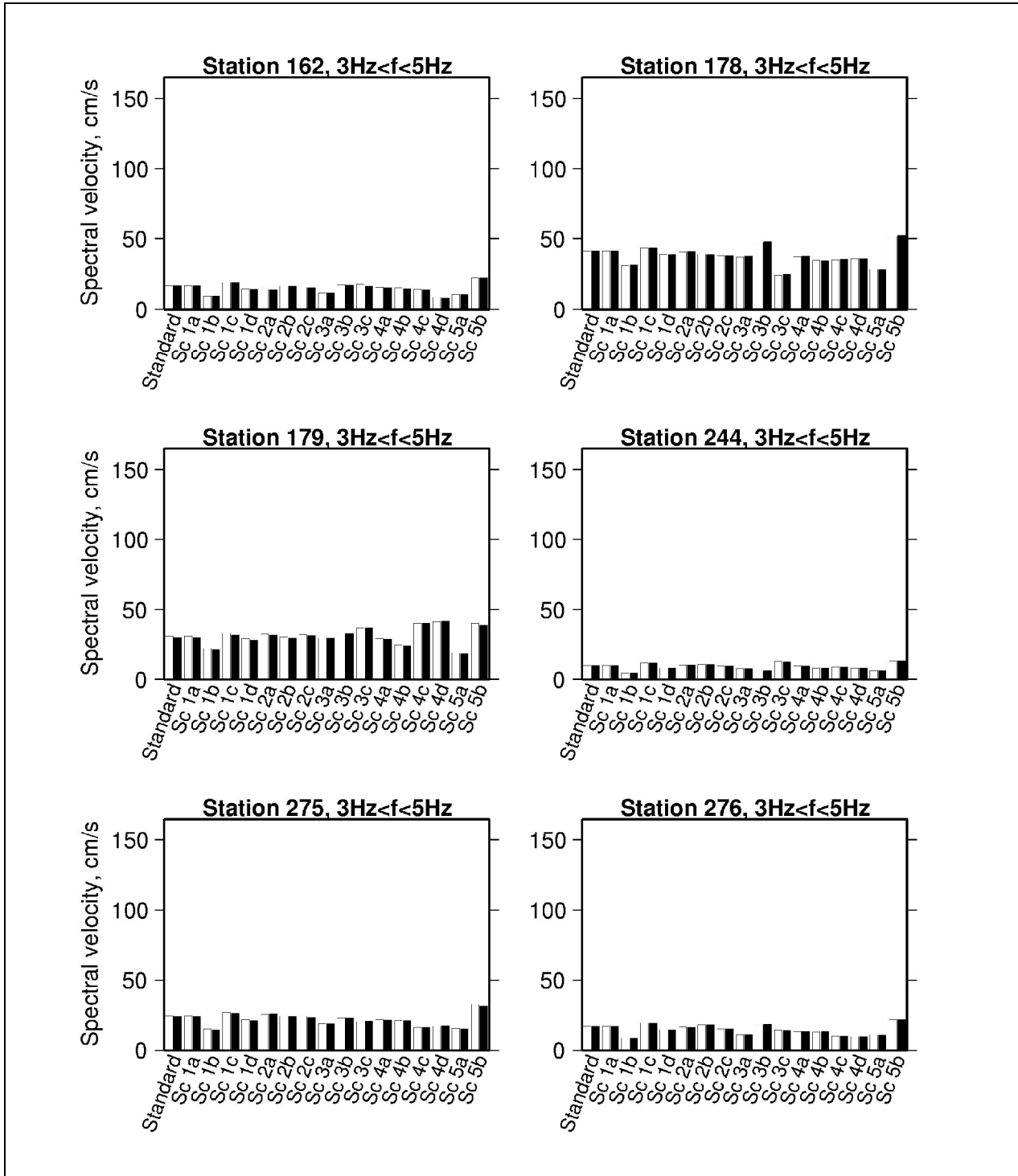


**Figure 3.2.22.** Spectral velocity at the sites in Figure 20 in the frequency band 3Hz<f<5Hz. White bars represent the NS component of the ground motion and black bars represent the EW component.



Project No: EVG1-CT-2002-00069

Deliverable no. 26 (Partner # 6: UiB)

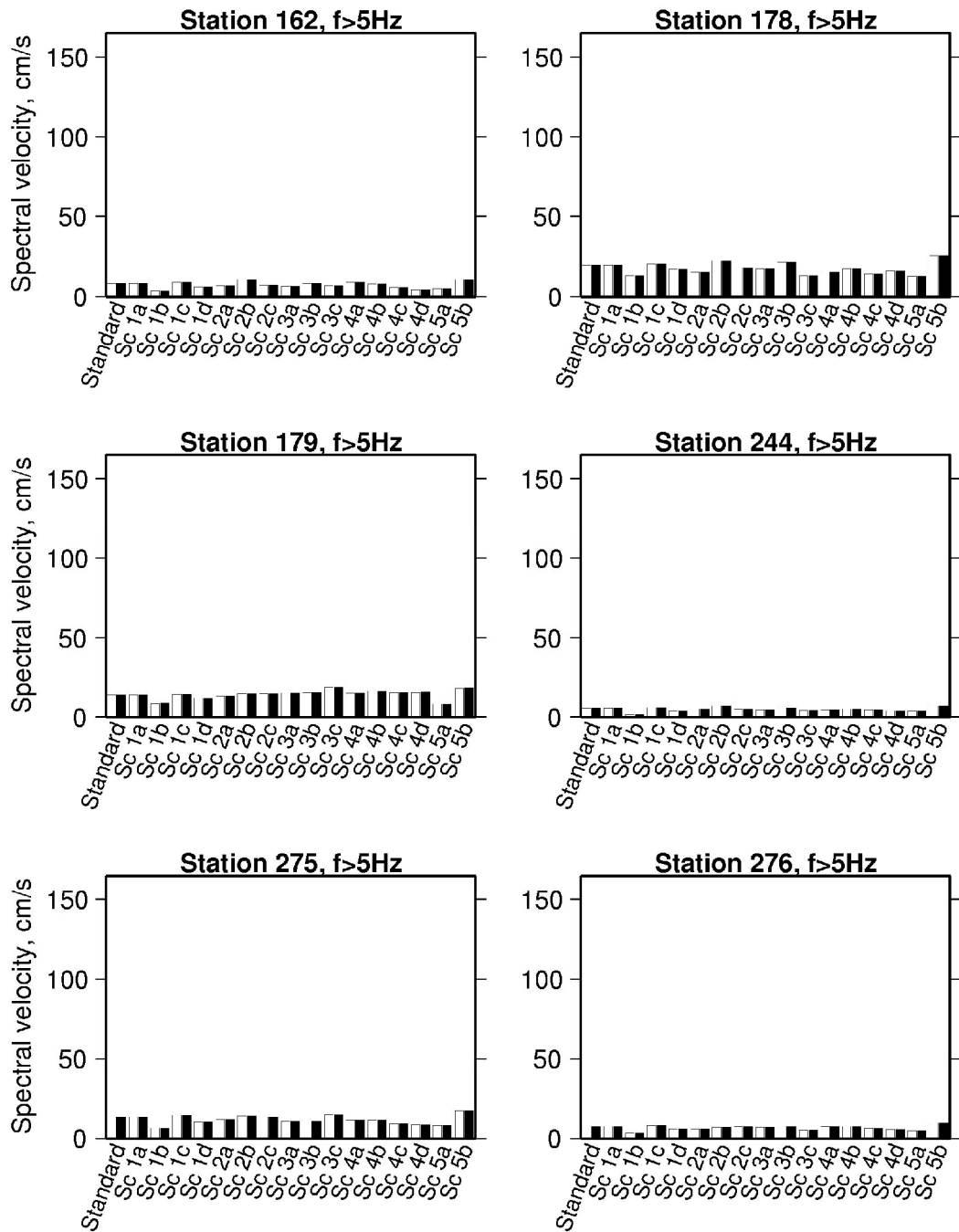


**Figure 3.2.23.** Spectral velocity at the sites in Figure 20 in the frequency band  $f > 5\text{Hz}$ . White bars represent the NS component of the ground motion and black bars represent the EW component.



Deliverable no. 26 (Partner # 6: UiB)



Project No: EVG1-CT-2002-00069

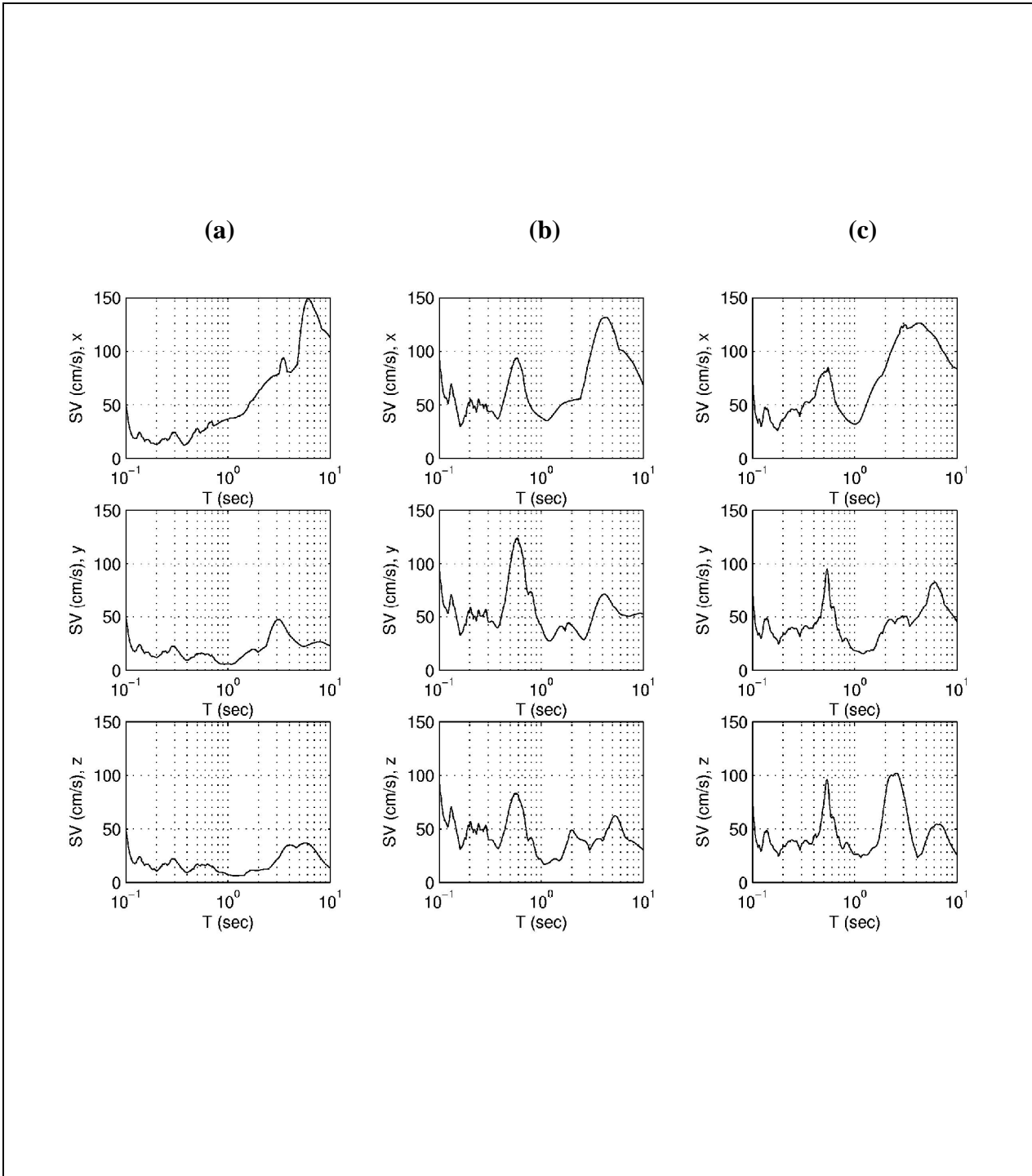


**Figure 3.2.24.** Velocity response spectra for the three components of ground motion using the standard scenario. x, y and z correspond to EW, NS and vertical, respectively. a) site 162, b) site 178, c) site 179.



Deliverable no. 26 (Partner # 6: UiB)



Project No: EVG1-CT-2002-00069

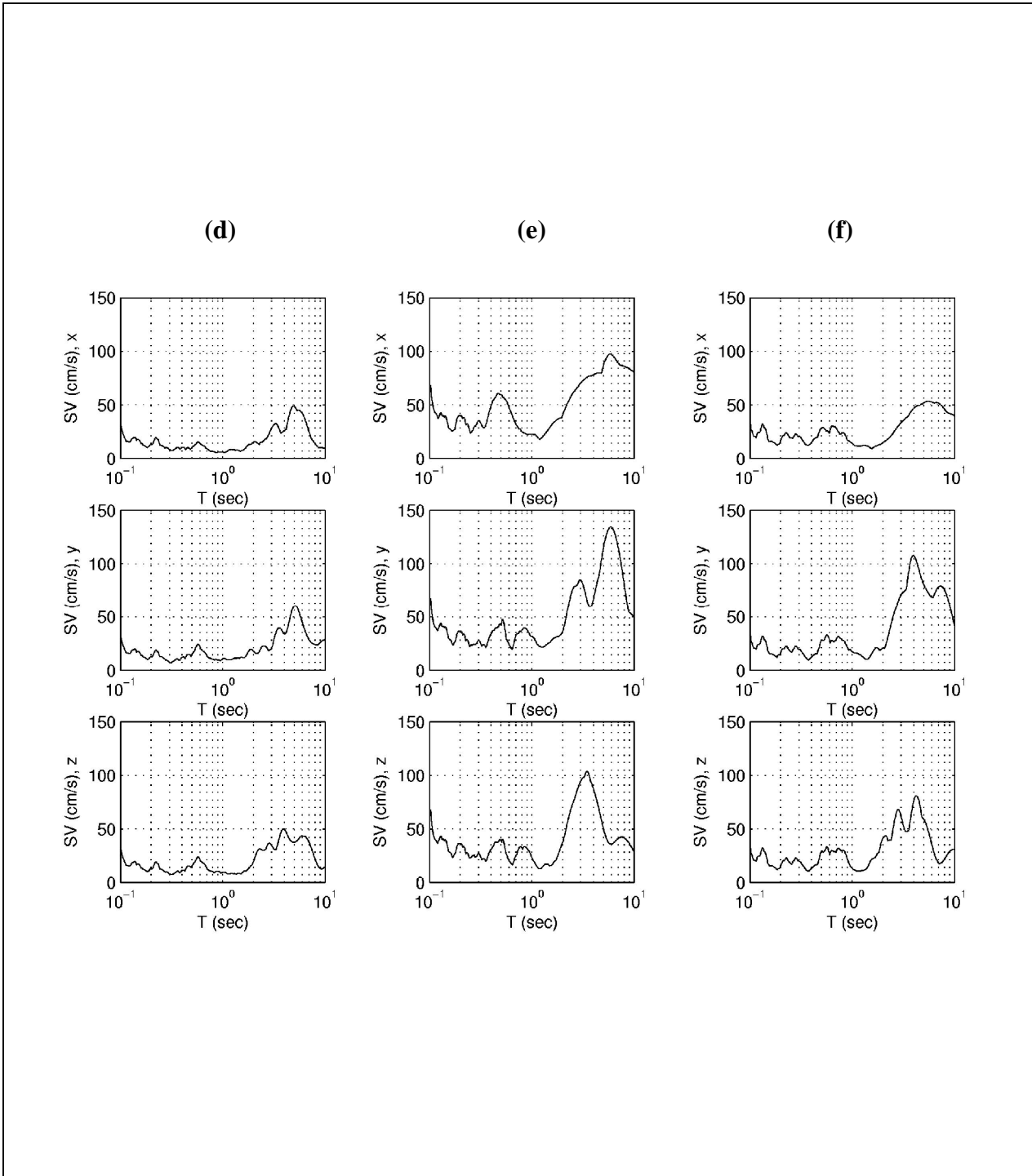


**Figure 3.2.24.** Velocity response spectra for the three components of ground motion using the standard scenario. x, y and z correspond to EW, NS and vertical, respectively. d) site 244, e) site 275, f) site 276.



Deliverable no. 26 (Partner # 6: UiB)



Project No: EVG1-CT-2002-00069

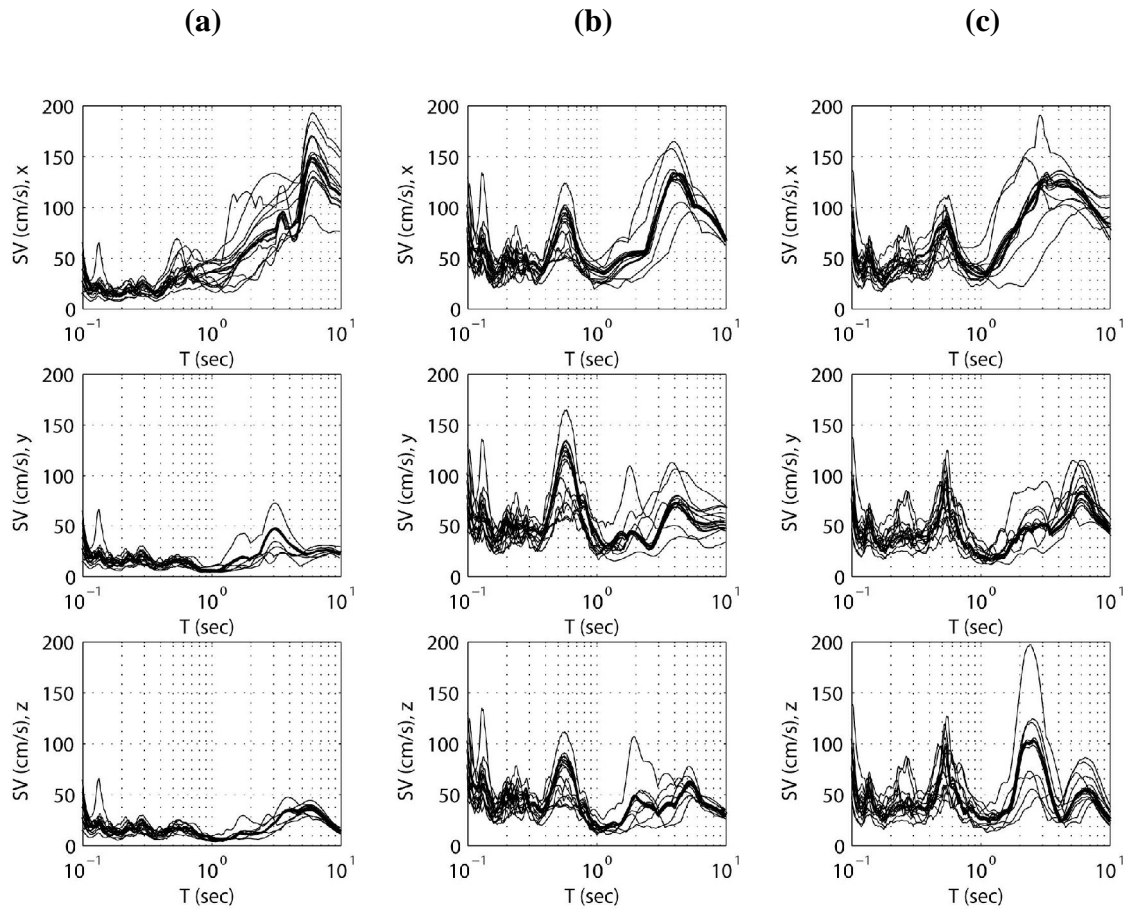


**Figure 3.2.25.** Comparison of the velocity response spectra for all 17 scenarios. All three components are shown. x, y and z correspond to EW, NS and vertical, respectively. The various scenarios are not differentiated in the plot since the aim is to show the variation and the upper and lower bounds of the spectra. a) site 162, b) site 178, c) site 179.



Project No: EVG1-CT-2002-00069

Deliverable no. 26 (Partner # 6: UiB)

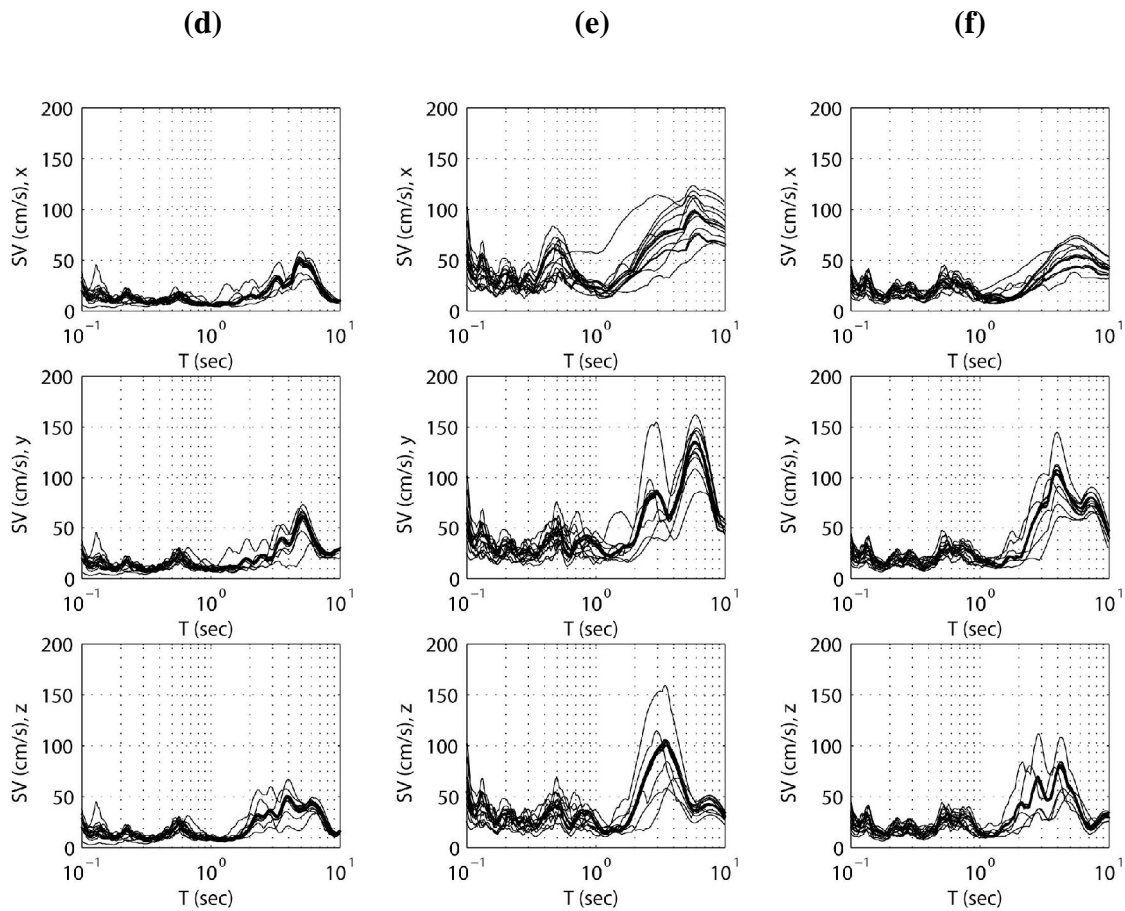


**Figure 3.2.25.** Comparison of the velocity response spectra for all 17 scenarios. All three components are shown. x, y and z correspond to EW, NS and vertical, respectively. The various scenarios are not differentiated in the plot since the aim is to show the variation and the upper and lower bounds of the spectra. d) site 244, e) site 275, f) site 276.



Deliverable no. 26 (Partner # 6: UiB)



Project No: EVG1-CT-2002-00069

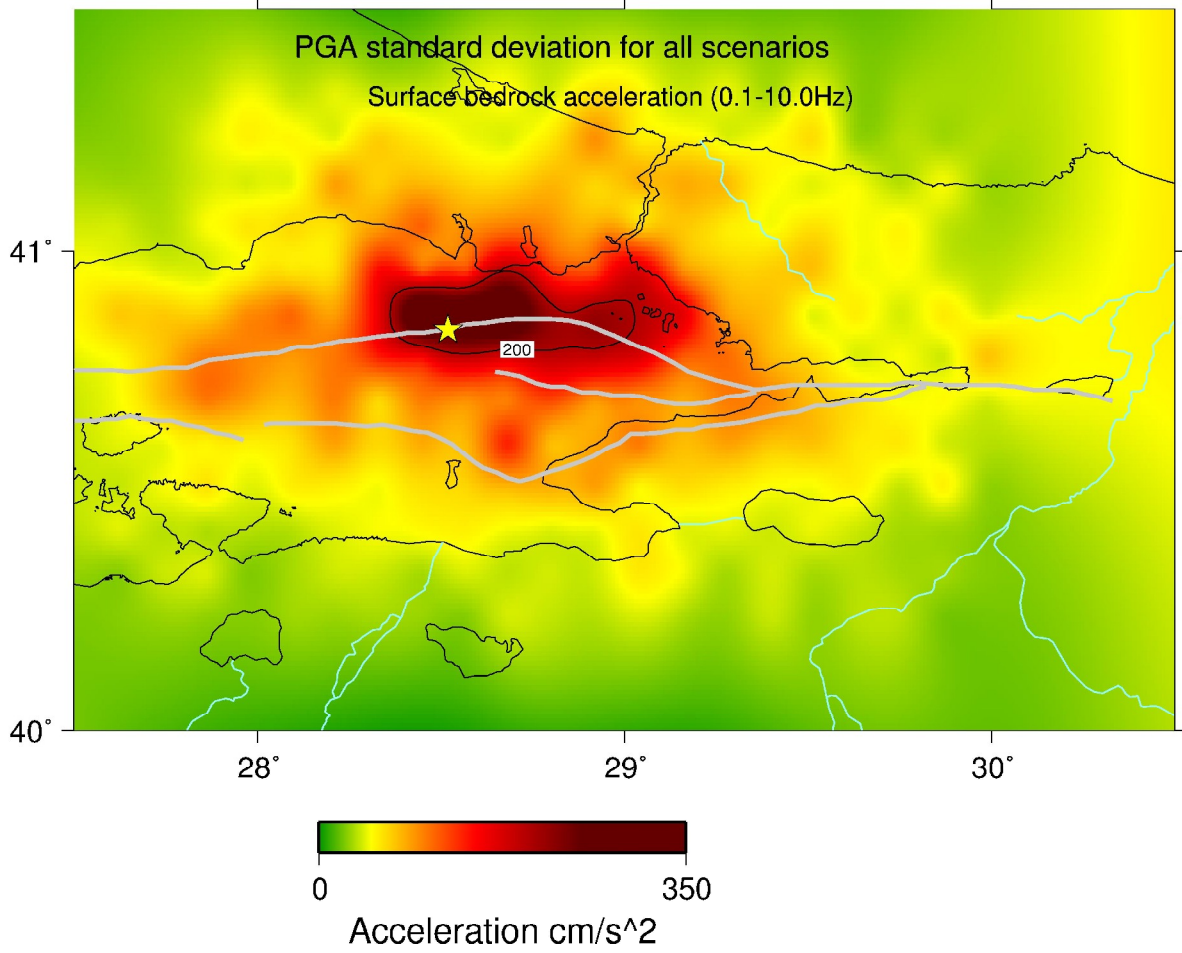


**Figure 3.2.26.** Distribution of the standard deviation for PGA for all 16 scenarios.

Deliverable no. 26 (Partner # 6: UiB)



Project No: EVG1-CT-2002-00069

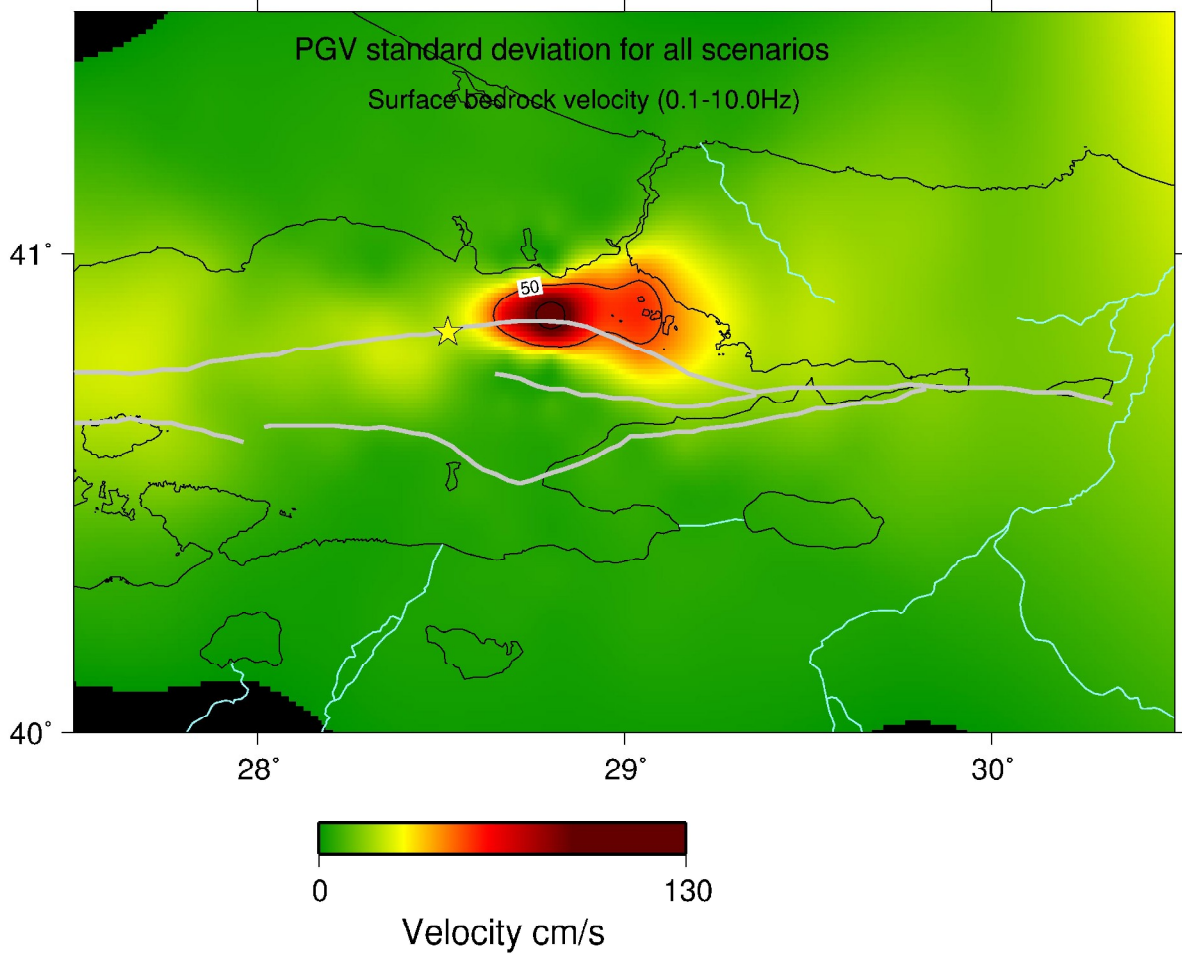


**Figure 3.2.27.** Distribution of the standard deviation for PGV for all 16 scenarios.

**Deliverable no. 26 (Partner # 6: UiB)**



**Project No: EVG1-CT-2002-00069**

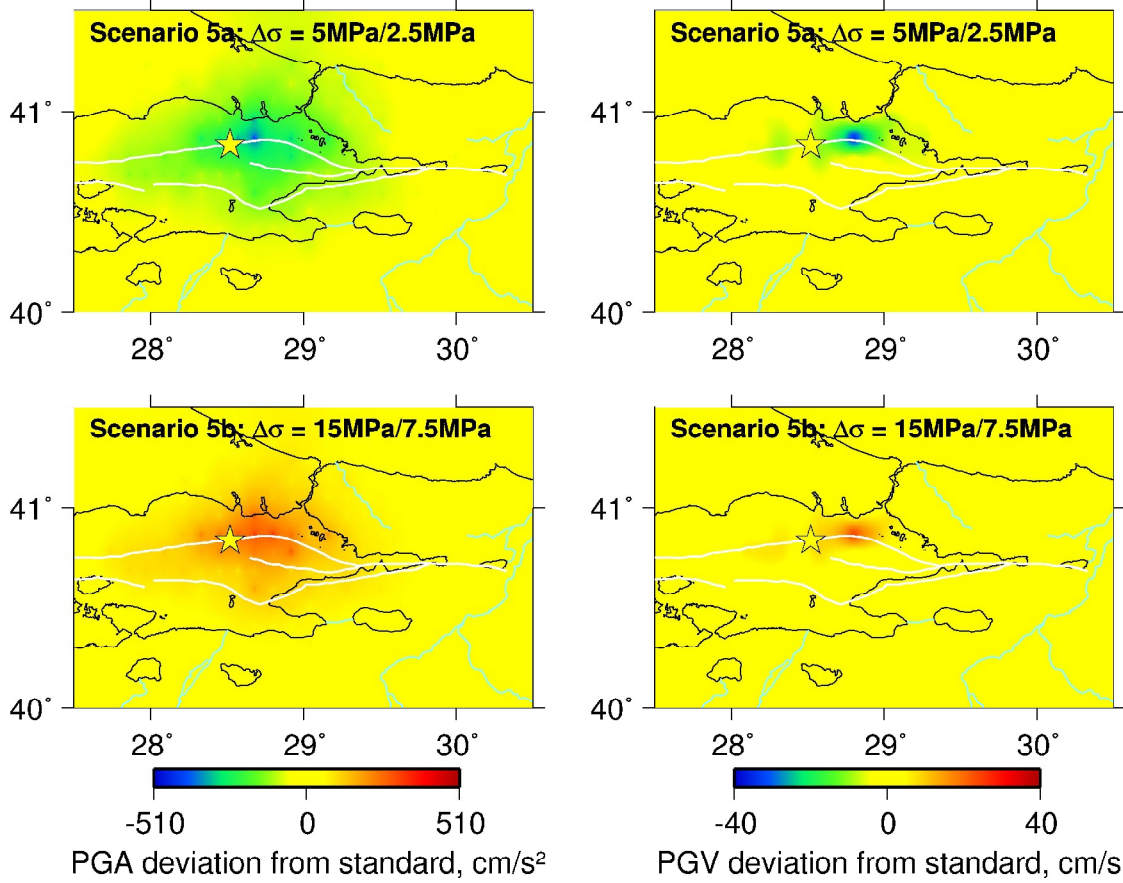


**Figure 4.1.** The figure shows the effect of stress-drop in terms of difference from the standard scenario by changing values for stress-drop. (PGA left and PGV right columns).



Deliverable no. 26 (Partner # 6: UiB)



Project No: EVG1-CT-2002-00069

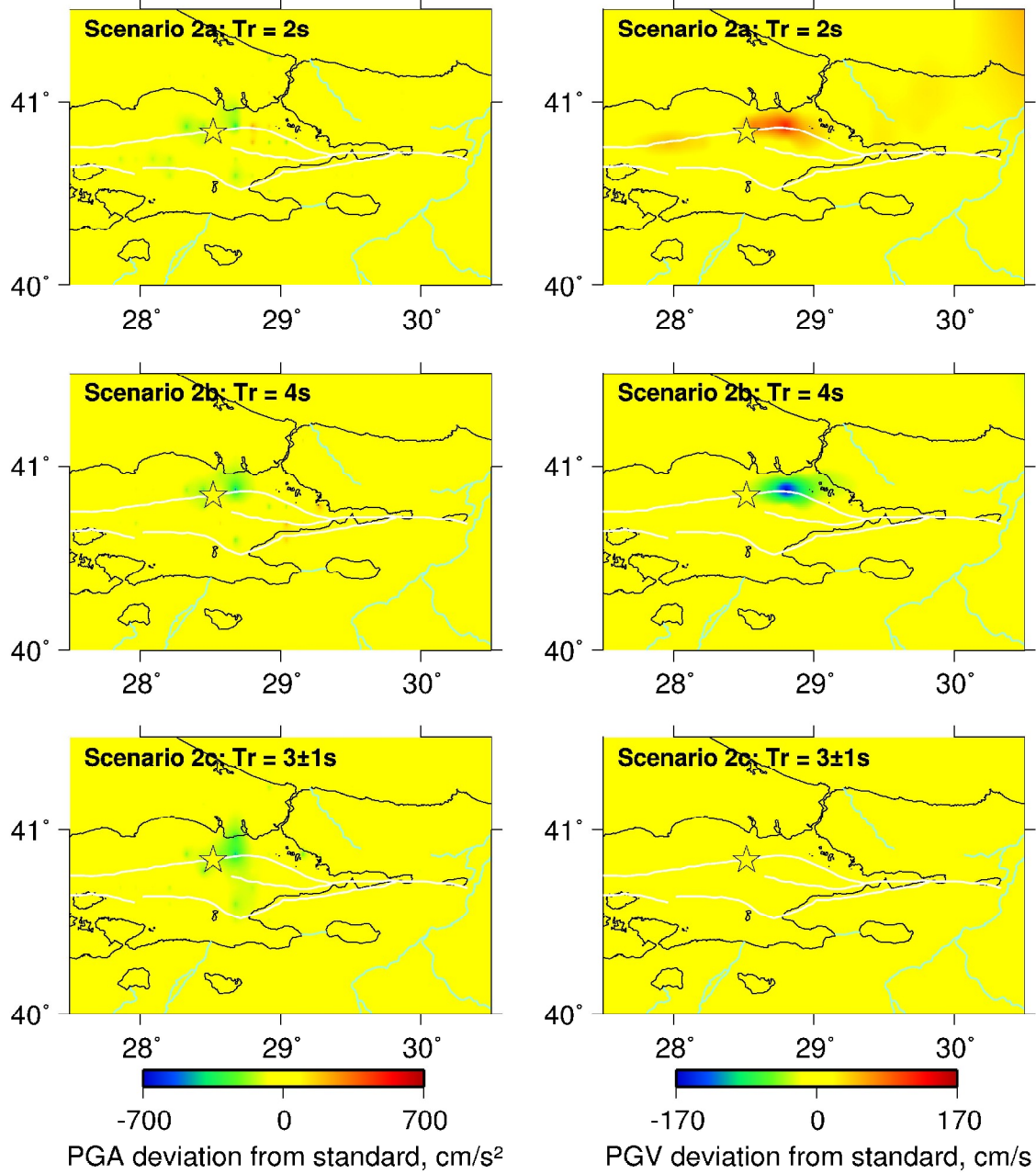


**Figure 4.2.** The figure shows the effect of rise-time in terms of difference from the standard scenario by changing values for rise-time. (PGA left and PGV right columns).

Deliverable no. 26 (Partner # 6: UiB)



Project No: EVG1-CT-2002-00069

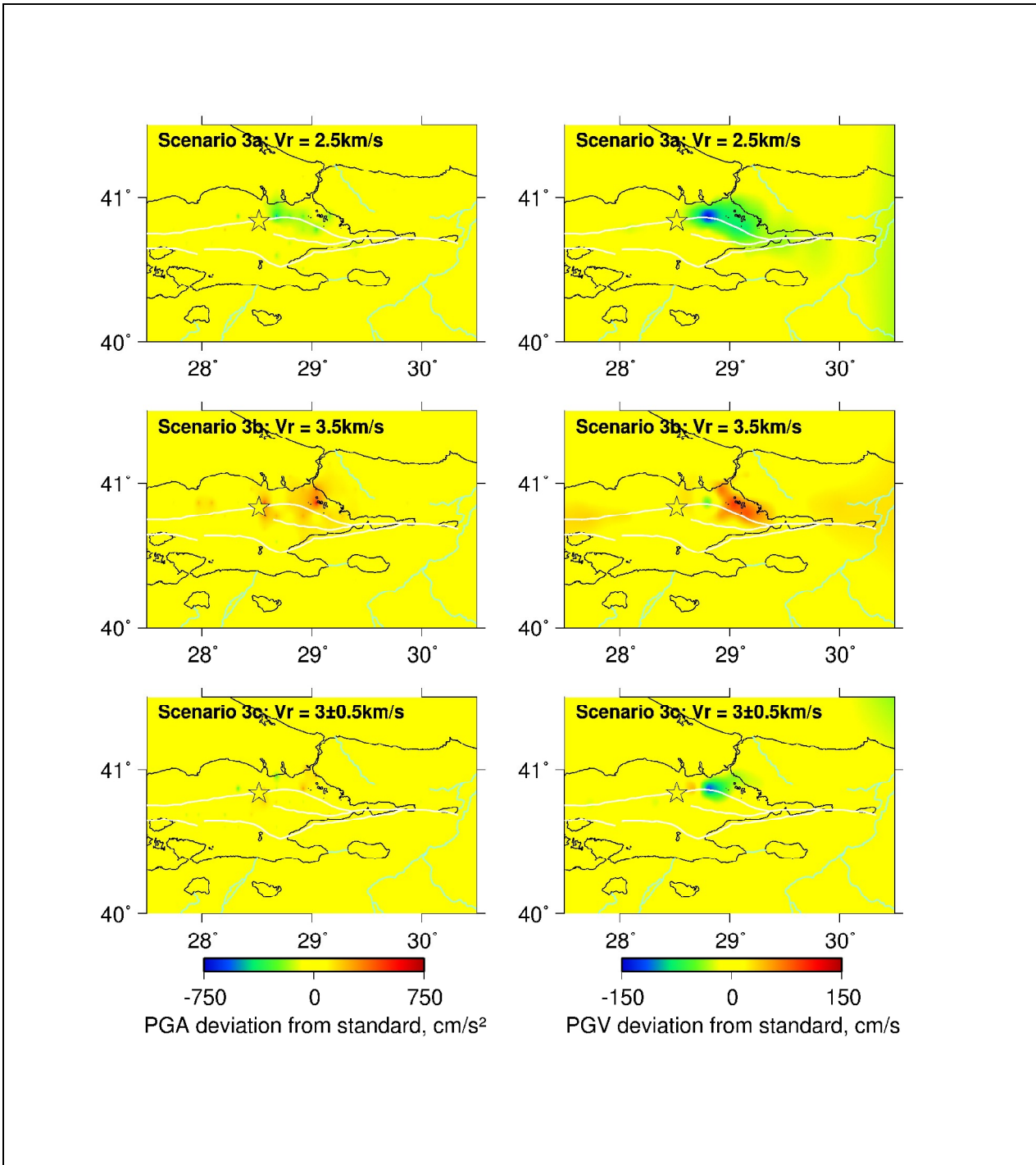


**Figure 4.3.** The figure shows the effect of rupture velocity in terms of difference from the standard scenario by changing values for rupture velocity. (PGA left and PGV right columns).



Deliverable no. 26 (Partner # 6: UiB)



Project No: EVG1-CT-2002-00069

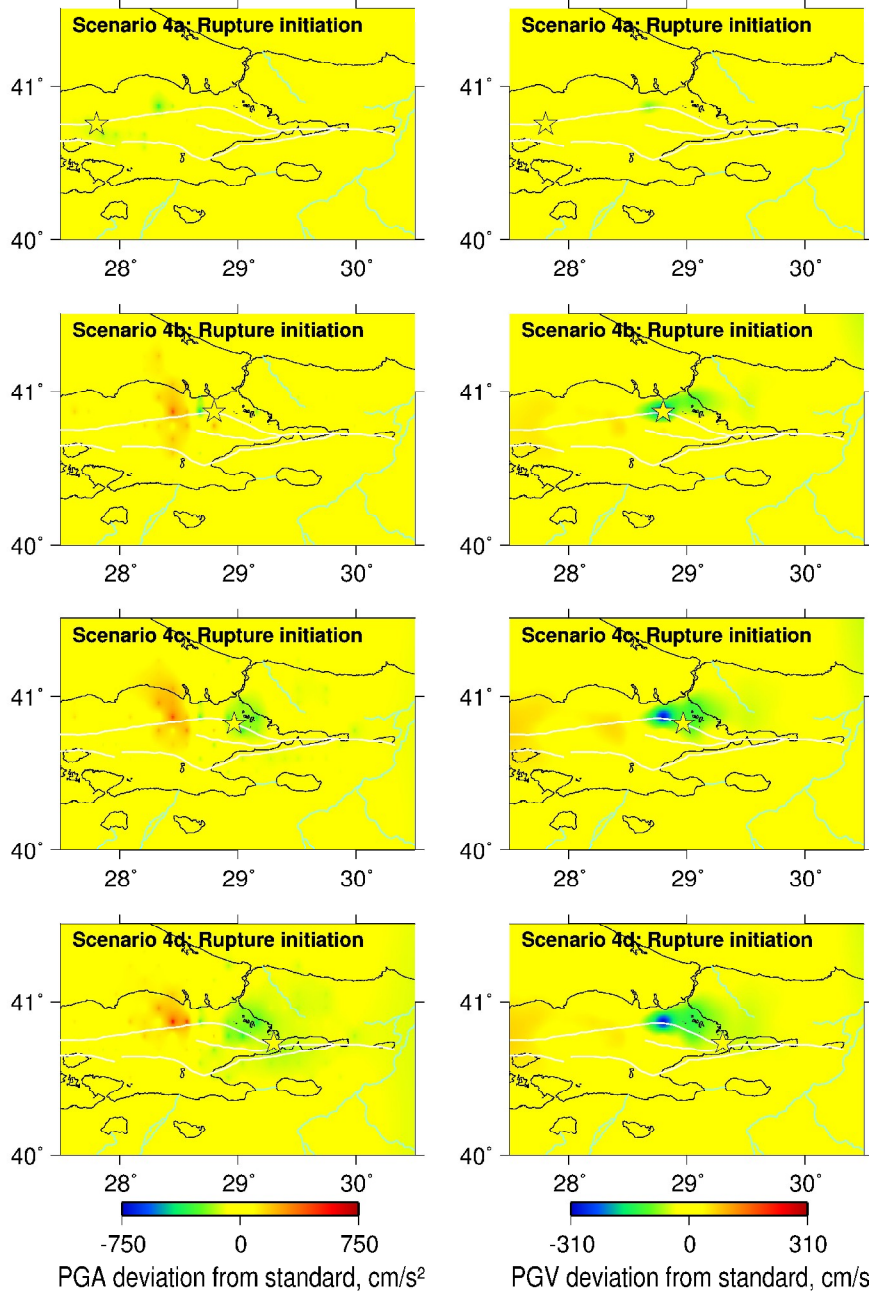


**Figure 4.4.** The figure shows the effect of rupture initiation in terms of difference from the standard scenario by changing rupture initiation point. (PGA left and PGV right columns).



Deliverable no. 26 (Partner # 6: UiB)



Project No: EVG1-CT-2002-00069

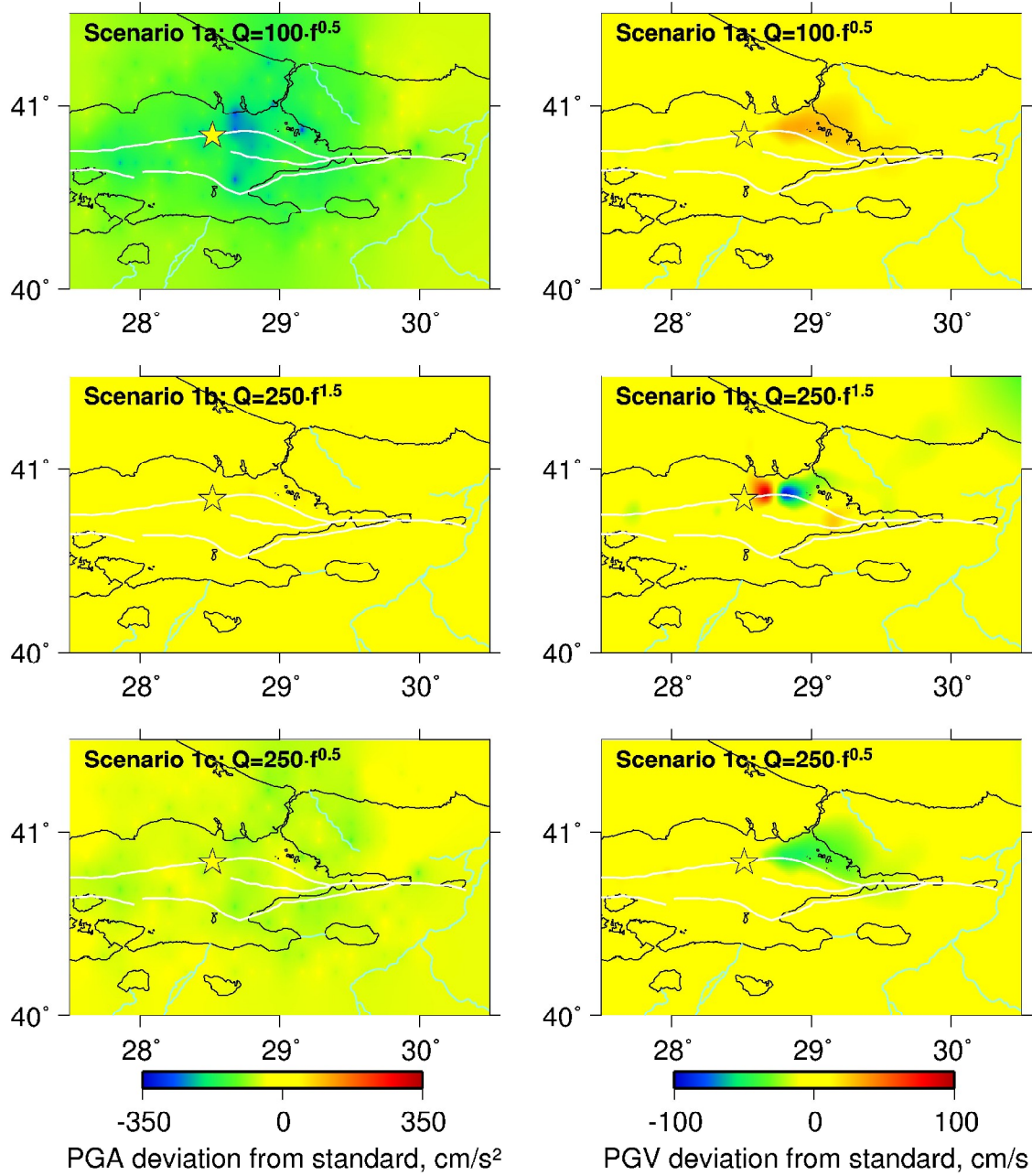


**Figure 4.5.** The figure shows the effect of attenuation in terms of in terms of difference from the standard scenario by changing the input values for Q. (PGA left and PGV right columns).

Deliverable no. 26 (Partner # 6: UiB)



Project No: EVG1-CT-2002-00069



This document was created with Win2PDF available at <http://www.daneprairie.com>.  
The unregistered version of Win2PDF is for evaluation or non-commercial use only.